



**Politecnico
di Torino**

DENERG Department of Energy “Galileo Ferraris”

Master’s Degree Course in Electrical Engineering

Master’s Thesis

in

Design of an Axial Flux Machine for a Micro-Wind Turbine

Student:

Irene Alberti

Supervisor:

Prof. Gianmario Pellegrino

Co-Supervisor:

Prof. Simone Ferrari

Academic Year 2024/2025

Abstract

This thesis focuses on the design of an Axial Flux Permanent Magnet Synchronous Generator (AFPMSG) for a micro-wind turbine. The benchmarking study wants to evaluate the performance of an existing generator, revealing the limitations in torque, power and also those derived from the high Joule losses, all confirmed through analytical evaluation.

For this reason two stator topologies were compared: a coreless stator and a PCB stator, both aimed at minimizing iron losses and enhancing efficiency.

The reference specification of the reference AFPMSG are the rated power of 350 W at 350 rpm, that correspond to a rated torque of about 12 Nm. The number of phases is three, while the motor have 10 poles, with a concentrated winding stator and two eternal rotors, for balance purposes.

While the coreless stator demonstrated higher efficiency and power density, it was less flexible and more expensive to manufacture. The PCB stator, in contrast, offered a more practical and scalable solution, maintaining acceptable performance while significantly reducing production complexity and cost.

The results highlight optimizing stator windings to improve power output and reduce losses. For the coreless solution the output power is a little more than duplicated (250W and 560W) and the joule losses are optimized at the 79%; for the PCB design, the output power is quite duplicated (250W and 433W) and the joule losses are optimized at the 50% if it is realized with 4 ounce of copper, 70% with 6 ounce of copper.

Ultimately it has been chosen the PCB design for its manufacturing advantages and cost-effective, performing through finite element analysis (FEA) simulations with FEMM 4.2, with additional optimizations carried out in Altium for PCB prototyping.

Future work could focus on thermal study, the cooling system of the PCB and exploring multi-layer configurations to improve efficiency. These findings confirm that PCB-based AFPMSGs are a feasible solution for cost-sensitive wind power applications, balancing performance, affordability, and ease of manufacturing.

Contents

Introduction	5
1 Axial Flux Permanent Magnet Synchronous Machines	6
1.1 Axial Flux Machine Structure	8
1.1.1 The two rotors	10
1.1.2 The stator	13
1.1.3 The generator under test	16
2 Benchmarking of the Available Generator	21
2.1 Generator Benchmarking and Analysis	23
2.1.1 Geometric Data and Dimensions	24
2.1.2 Test at Constant Motor Speed	35
2.2 Benchmarking Results and Comments	38
2.3 New Generator Specs	39
3 Design of the New Generator	41
3.1 Coreless Stator Sizing	43
3.1.1 Sizing equation	46
3.2 PCB Stator Sizing	49
3.2.1 Sizing equation	53
3.2.2 Parameters optimization	57
3.2.3 Multi-Objective Optimization	58
3.2.4 Final results	59
3.2.5 2D Analysis - FEA	64
3.2.6 Design on Altium	68
3.3 Technologies Comparison and Selection	71
Conclusions	80
Appendix	82
Bibliography	101

List of Figures

1.1	Linear simple schematic	7
1.2	Rotor and Generator	7
1.3	Axial and Radial flux direction [1]	8
1.4	Generator under study	9
1.5	The rotor of AFPMS actual generator under study	11
1.6	The stator of AFPMS actual generator under study	13
1.7	Curve C_P - TSR	18
1.8	Curve $C_P - V_{wind}$	19
1.9	Curve $P_m - V_{wind}$	20
1.10	Power and Torque requested	20
2.1	Curve Graph	22
2.2	Geometric dimension of the stator	24
2.3	Geometric dimension of the stator	25
2.4	Geometric dimension of the rotor	25
2.5	Geometric dimension of the rotor	26
2.6	Test Bench	27
2.7	Joule Losses	28
2.8	Test setup with the supply	31
2.9	Test setup with thermographic camera	32
2.10	One side of the stator	33
2.11	The other side of the stator	33
2.12	Generic schematic of the test	36
2.13	Bench of the load test	36
2.14	a) load and speed measured; b) Power and speed - color scale: the load range in resistance [Ω]	37
3.1	Winding with Dolomites	44
3.2	Coreless stator winding	45
3.3	Types of PCB[2]	52
3.4	Magnetic field in the air gap	54
3.5	Dolomites for PCB	56
3.6	Pareto Front analysis	59
3.7	Number of traces for a single layer	61
3.8	Trend with varying copper traces	62

3.9	Trend with varying copper traces with double layer	63
3.10	Number of traces for a double layer	64
3.11	2D model	65
3.12	2D details	66
3.13	FEMM 2D	66
3.14	FEMM 2 poles	67
3.15	Windings PCB details with Dolomites	68
3.16	PCB with 480 traces on Altium	69
3.17	Detail of the sensors	70
3.18	3D view of Altium	71
3.19	Joule Losses for PCB structure	73
3.20	Joule Losses for coreless structure	73
3.21	Comparison between the two technologies	74
3.22	Comparison between the two technologies for electromagnetic fields.	75

List of Tables

- 1.1 Specification Table 10
- 1.2 Properties of N42H Magnets[3] 12

- 2.1 Resistance measurement of a winding. 28
- 2.2 Results of EMF-test 29
- 2.3 Main parameters 39
- 2.4 Parameters of the rotor 40
- 2.5 Parameters of the magnets 40

- 3.1 Parameters 57
- 3.2 First Range of parameters for PCB Design 58
- 3.3 New Range of Parameters for PCB design 60
- 3.4 Final PCB design 68
- 3.5 Comparison of Coreless and PCB Stators 77

Introduction

The increasing demand for green energy alternatives has contributed to the rising popularity of micro wind turbines as one of the many possible sources of decentralized electricity. Axial Flux Permanent Magnet Synchronous Generators (AFPMSGs) have attracted much interest in the last years thanks to their small, high-efficiency, and direct-drive system eliminating the gearbox and reducing mechanical losses. This work wants to design and optimize an AFPMSG for a small wind turbine, the product of the EoliTo team at Politecnico di Torino. The first target is to analyze the performance of the existing generator, which was diagnosed as inefficient, mainly due to excessive Joule losses and poor torque generation at low speeds. Two different stator topologies were therefore compared: the coreless stator, high in efficiency but at a greater cost and more complex; the PCB stator, which offers a more cost-effective and scalable solution.

The study includes analytical modeling, finite element simulations (FEMM 4.2), and PCB prototyping (Altium) to compare the two approaches and identify the most suitable configuration for the application.

The thesis is structured as follows:

- Chapter 1 provides an overview of AFPMSG technology and its relevance to wind power applications.
- Chapter 2 presents a benchmarking analysis of the existing generator, highlighting its limitations and introducing the new specs.
- Chapter 3 details the design and simulation of the new generator, comparing coreless and PCB stators and making a choice, discussing about its implication and potential improvements and possible future work.

The results of this study confirm that PCB-based AFPMSGs can provide a practical and cost-effective alternative for micro wind turbines, balancing performance, manufacturability, and affordability.

Chapter 1

Axial Flux Permanent Magnet Synchronous Machines

Electrical motors serve as the cornerstone of both industrial and commercial operations. As a result, advancements and innovations in motor technology are constantly evolving. Motors generate rotational or linear motion through the interaction of two magnetic fluxes. These machines can be broadly categorized into conventional types, such as DC motors, induction motors, and synchronous motors and other specialized electrical machines, including Switched Reluctance Motors (SRM), Synchronous Reluctance Motors (SynRM), among others. Most of these motors fall under the category of radial machines[4].

However, there is another unique category of motors known as Axial Flux Machines (AFM), which is made up by permanent magnet, in all the different configurations (internal, external, surfaced, Halbach, etc).

The Axial Flux Synchronous Machines with Permanent Magnets have gained significant attention in recent years due to their high efficiency, compactness, and suitability for various applications, wind power generation stands out among the many applications.

The projects want to focus on the design and sizing of such a generator, specifically intended to power a small wind turbine developed by the Eolito team.

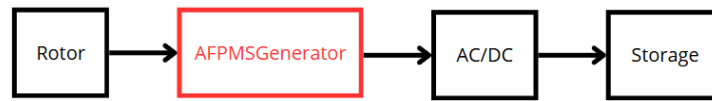


Figure 1.1: Linear simple schematic

Moreover, the axial flux generator is employed in these applications as it eliminates the need for a gearbox, owing to its capability to achieve very high rotational speeds. However, in this specific case, given the nature of a micro-wind turbine, such high speeds will not be attained due to the limitations imposed by the structural design of the rotor.

Initially, a preexisting generator belonging to the team was studied to evaluate its performance characteristics: this generator demonstrated certain strengths, as it lacked sufficient torque to meet the requirements of the micro-wind turbine.

This limitation highlighted the need for a redesigned solution capable of delivering higher torque while maintaining efficiency and compactness.

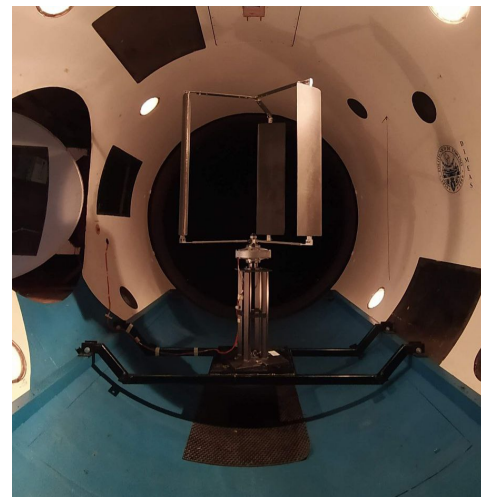


Figure 1.2: Rotor and Generator

In this chapter, the fundamental principles of the axial flux synchronous generator will be introduced, along with an overview of the challenges and objectives that guided the development of the project.

1.1 Axial Flux Machine Structure

The Axial Flux Permanent Magnet Synchronous Motors (AFPMSM) is characterized by a magnetic flux oriented along the machine's axial direction. In conventional radial flow machines, the flux in the air gap is directed radially, while in axial flow machines, it follows the axial direction.

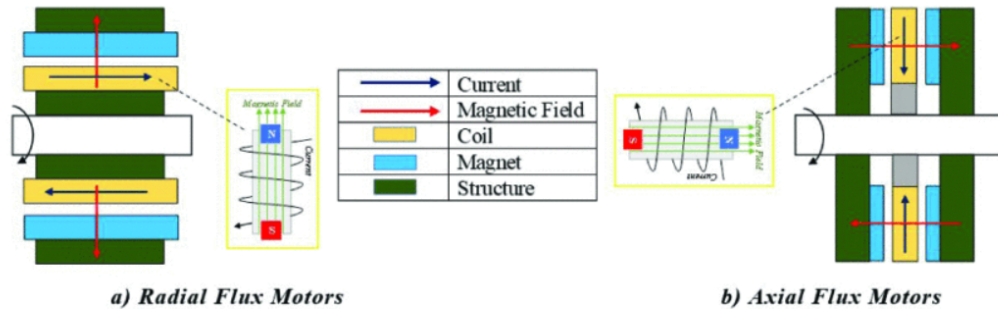


Figure 1.3: Axial and Radial flux direction [1]

The torque generating surfaces — where conductors and permanent magnets are positioned — are placed perpendicularly to the axis. This design enables the machine to achieve high specific torque values, as the active components are placed near the outer circumference, maximizing the distance from the axis of rotation. Additionally, the use of permanent magnets to generate the field allows for the construction of a synchronous machine with a torque output directly proportional to the number of pole pairs. In axial flow machines, unlike their radial counterparts, the torque increases proportionally with the number of poles.[5].

The AFPMSM in the last decades are increasingly used because of their higher power density than their radial flux equivalent, their light-weight and, in the specific application of this context, they are very interesting for the possibility of direct connection to the wind turbine which limits the losses by removing the gear box [6].

There are numerous types of axial flux motors (single rotor-single stator, double rotor-single stator, double stator-single rotor, multi rotor-multi stator, etc.), each designed for specific applications and operating principles.

In this thesis, however, the focus will be on a specific configuration: a double-rotor single-stator design, which has been selected as the subject of this study.

Despite the other types, the main qualities of this type of structure are:

- lower iron and copper losses,
- high power density,
- the rotation of the rotating parts around the stators winding work as cooling fans for the windings[7],
- the balanced magnetic attraction between rotors and stators.

Obviously it has also some disadvantages. For example, the effective air gap area is larger than double-stator single-rotor machine and this influences the magnetic field generated.

The structure under study is composed by:

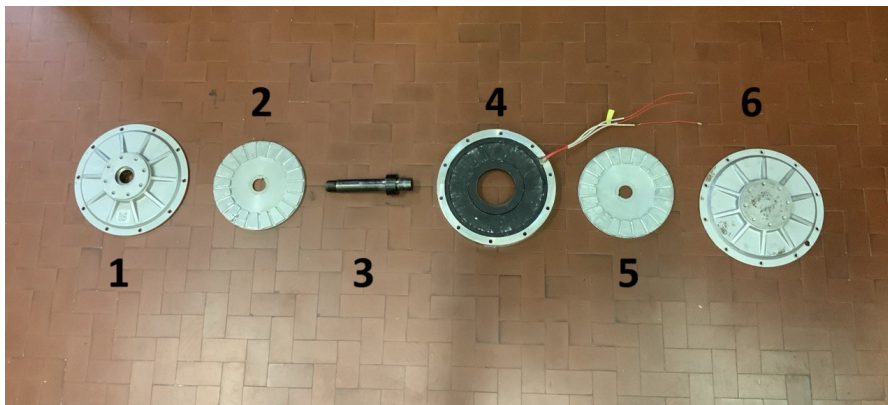


Figure 1.4: Generator under study

- 1 and 6 are the case in aluminum,
- 2 and 5 double rotor,
- 3 the shaft,
- 4 the stator.

as it can be seen in the figure 1.4.

The main specifics of the generator are:

- The machine is ten pole pair;
- Three-phase, synchronous generator with permanent magnets (PM);

- The PMs are collocated on both rotors and they are covered with a protective coatings to prevent mechanical hurts;
- The stator is slot-less and coreless (after will be better explained);
- Both rotors are made with steel, unless the magnets.

Here are the specifications reported by the manufacturer.

Parameters	Unit	Value
Rated power	kW	0.25
Rated speed	rpm	200
Rated voltage	V	24VAC
Rated Line Current	A	6.01
Efficiency		>85%
Resistance (Line-Line)		-
Winding type		Y
Insulation Resistance		100M Ω Min (500V DC)
Leakage level		<5 mA
Start torque	Nm	<0.1
Phase		Three phase
Structure		Inner rotor
Stator		coreless
Rotor		PM type (Inner rotor)
Housing Material		Aluminum (Alloy)
Shaft Material		Steel
Gen. Diameter	mm	265
Gen. Length	mm	104
Shaft Diameter	mm	30
Net Weight	kg	13
Gross Weight	kg	16

Table 1.1: Specification Table

1.1.1 The two rotors

Both rotors are composed with 20 magnets N42H: these types of magnets are sintered Neodymium-Iron-Boron (NdFeB) magnets.



Figure 1.5: The rotor of AFPMS actual generator under study

They are known for their high magnetic output combined with moderate cost, making them suitable for various applications. They are also versatile, offering a balance of magnetic strength, temperature resistance, and physical durability, making them suitable for uses in motors, sensors, and various industrial assemblies.

An interesting factor to consider is that axial flux machines typically have magnet heights equal to the magnetic path length, but this is not the case here. This choice was likely made to reduce costs, making the generator more competitive in price. Additionally, the selected magnets have a strong magnetic pull, which might compensate for the shorter-than-usual length.

Property	Value
Residual Induction (B_r)	1.28 - 1.32 T
Coercivity (H_{cB})	955 - 1003 kA/m
Intrinsic Coercivity (H_{cJ})	1.353 kA/m
Maximum Energy Product (BH_{max})	318 - 342 kJ/m ³
Thermal Characteristics	
Temperature Stability ($\alpha(B_r)$)	-0.12%/°C
Temperature Stability ($\alpha(H_{cJ})$)	-0.57%/°C
Curie Temperature (T_c)	310°C
Thermal Conductivity	5.3 - 5.8 kcal/m·hr·°C
Physical Properties	
Density	7.6 g/cm ³
Flexure Strength	285 MPa

Table 1.2: Properties of N42H Magnets[3]

1.1.2 The stator

In this generator, the stator has two main characteristics: it is coreless and slot-less.

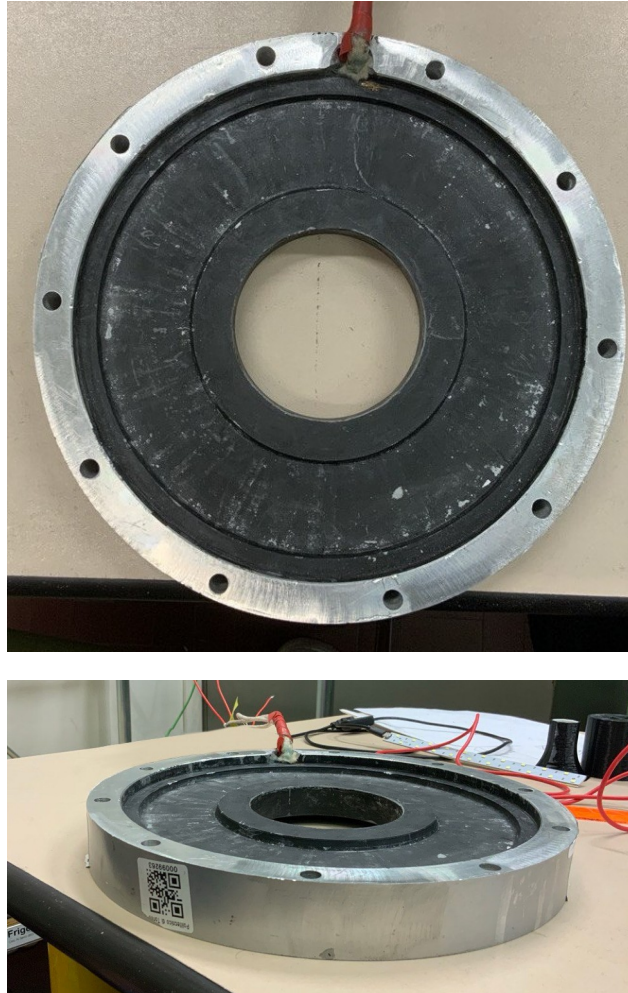


Figure 1.6: The stator of AFPMS actual generator under study

Starting with the first property, the absence of stator cores is a notable characteristic of certain AFPM machine designs, offering multiple advantages but also some disadvantages:

- The absence of a core plays a key role in reducing magnetic losses, weight, and production complexity, simplifying the machine's overall structure.
- The resulting machine is more compact and lightweight, which is especially beneficial in applications where minimizing space and weight is

crucial.

- Without a stator core, these machines achieve a higher power density, meaning they can produce more power in a smaller, lighter form factor compared to traditional designs.
- Traditional stator cores are subject to eddy current losses caused by fluctuating magnetic fields. By eliminating the core, these losses are significantly reduced, improving overall efficiency.
- The simpler construction makes it easier to adapt the machine for specific applications.
- Despite the simpler design, the absence of a stator core introduces new manufacturing complexities, such as the need for precise coil winding and assembly. Advanced techniques may be required to ensure proper alignment and component placement.
- Without a stator core to guide the magnetic flux, challenges can arise with field distribution. Careful design and optimization are essential to maintain efficient magnetic performance. Additionally, the larger air gap due to the absence of magnetic material necessitates the use of more permanent magnet material compared to a machine with a ferromagnetic stator core.
- AFPMs without stator cores may require custom control algorithms to optimize performance and efficiency, accounting for the unique behavior of the magnetic field in this design [8].

Moreover, the stator is also slot-less, which implies:

- In addition to the absence of a ferromagnetic core, the lack of slots further reduces the torque density compared to slotted motors. Stronger magnets or larger dimensions may be needed to achieve comparable torque.
- Since the windings are distributed without slots, a larger amount of copper is needed to achieve the same current density as in a slotted motor, increasing material costs. Additionally, the windings are often longer to generate the required magnetic field, leading to higher total resistance losses.

- On the other hand, the slot-less windings are designed to achieve low values of self-inductance and phase inductance. As a result, the required electromotive forces (EMF) can be generated with fewer winding turns, which decreases both resistance and inductance, ultimately improving the overall voltage quality.

The combination of high-performance permanent magnet materials with slot-less windings results in a highly compact machine that facilitates efficient air cooling of active components. The primary advantage of the slot-less configuration is its higher overall efficiency.

On the other hand, the slotted configurations introduce undesirable effects such as flux ripple, tooth losses, and cogging torque. However, they also offer advantages, including greater structural robustness and a smaller effective air gap [7].

Moreover the slot-less toroidal stator PM configuration features a simple toroidal strip-wound stator core that supports a slot-less toroidal winding. Various tests have demonstrated its steady-state reliability and high performance when used as both a generator and a motor[7]. The machine's configuration depends on the relative magnetization orientation of the permanent magnets (PMs).

- In the north-north (NN) configuration, magnets with opposite magnetization face each other. Here, the flux path closes through the stator yoke, making the stator core essential. However, the slot-less stator design introduces the challenge of an increased effective air gap length, as the coils occupy space within the air gap.
- In the north-south (NS) configuration, the north pole of one rotor faces the south pole of the opposing rotor, and vice versa. This results in an entirely axial flux path between the two rotors. Consequently, the inner stator core becomes unnecessary, enabling a coreless slot-less machine design.

Once the motor was fully disassembled (it will be explained in paragraph 2.1), it has been verify the polarity of the configuration: the magnets are disposed with North-South (NS) configuration, as evidenced by their strong attractive force; the two rotors were strongly attracted to each other.

By leveraging the advanced properties of permanent magnets and the coreless,

slot-less configuration, the motor harnesses material potential to achieve high efficiency and compactness. However, these design choices involve compromises: while the slot-less configuration is more compact and offers the aforementioned advantages, it significantly increases Joule losses. Despite this, the EMF generated by these types of windings is sufficiently high. Moreover, the strength of the magnets helps offset the disadvantages of the coreless and slot-less configuration, ensuring a high magnetic field density.

The windings have drawn particular attention during the analysis. Encased in a black insulating material, their exact configuration was initially unclear. A thorough literature review was conducted to deduce the type of windings employed. The preliminary hypothesis was that the windings are concentrated, with a reduced number of turns. This assumption aligns with the design optimization of this motor, as discussed previously, which requires only a few turns to achieve an EMF equivalent to that of a slotted motor.

Additionally, insights from the study [9] suggest that for this type of motor configuration, and to ensure a competitive cost-performance ratio, preformed concentrated windings are often utilized. These pre-manufactured windings help maintain high performance while reducing manufacturing complexity and costs, making the motor more viable in competitive markets.

In any case, further considerations will be addressed in the following chapter 2.

1.1.3 The generator under test

In the table 1.1, there are represented all the characteristics known of the generator.

The generator presented thus far does not meet the specifications required by the team, because it was chosen based on old specifications of a rotor that has since been improved. Specifically, a generator capable of maintaining a rotational speed at 350 rpm while achieving quite the same torque output is needed. The following graphs, developed by the aerodynamics section of the team, provide detailed insights into the performance characteristics and underlying requirements for this improved design.

In the following graphs, it can be seen the curves that have been studied.

The first one (Fig. 1.7) represent the C_p (power coefficient) and TSR (tip-speed ratio) curves, that are crucial for wind turbine analysis:

- C_P : It represents how efficiently the wind turbine converts wind energy into mechanical energy. This efficiency peaks at a specific TSR. To maximize energy capture, the generator must operate near this optimal TSR for the given wind speeds. The efficiency of converting wind energy to mechanical energy is defined as

$$C_P = \frac{P_{\text{mechanical}}}{P_{\text{wind}}}, \quad P_{\text{wind}} = \frac{1}{2}\rho Av^3. \quad (1.1)$$

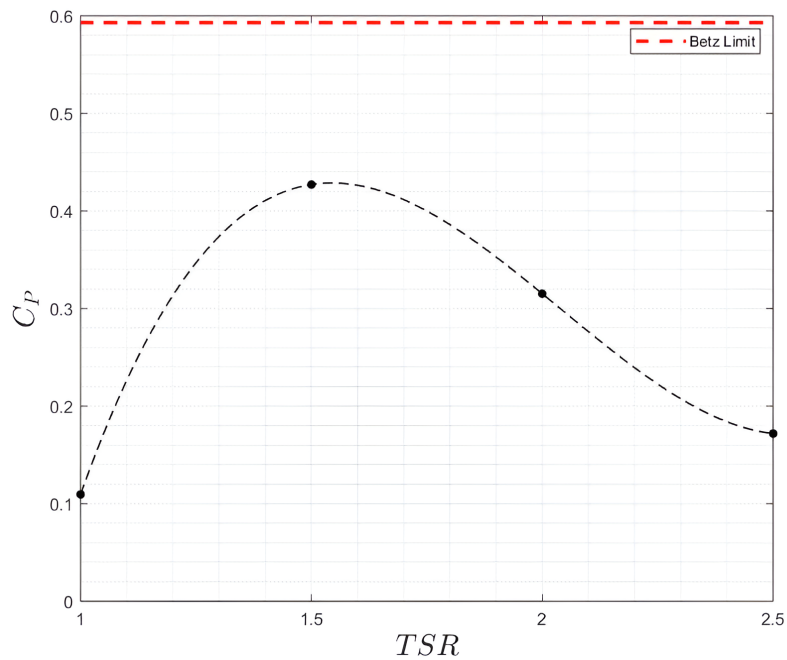
where ρ is the air density, A is the area that cover the three vertical axis of the rotor and v is the wind speed.

- TSR : The TSR is determined by the rotor's speed relative to wind speed. The generator's electrical characteristics (e.g., voltage and current output at certain speeds) must align with the rotor's speed range, especially near the TSR where C_P is maximized. The ratio of blade tip speed to wind speed is defined as

$$TSR = \frac{\omega R}{v}, \quad (1.2)$$

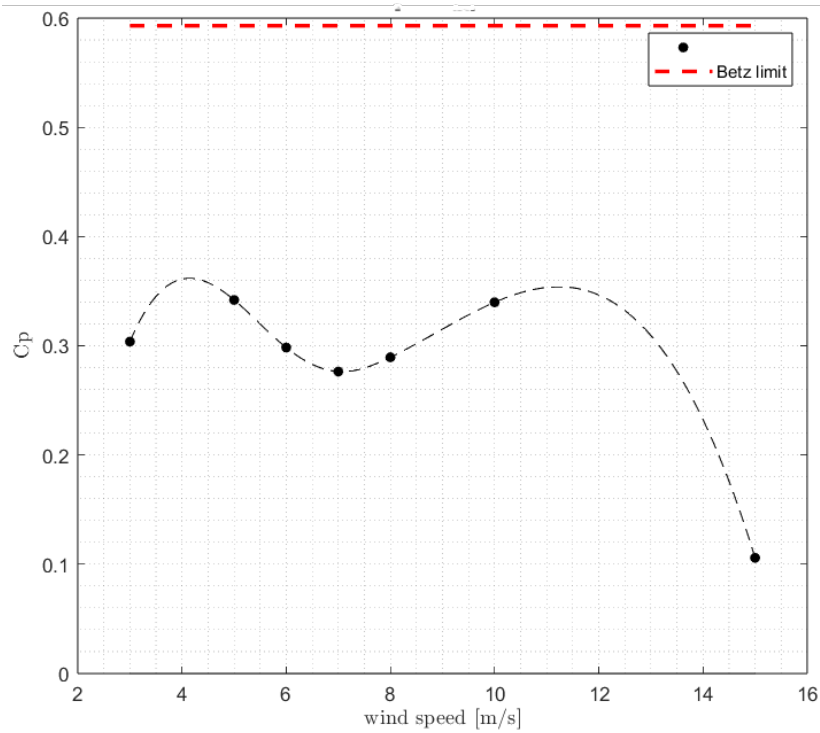
where ω is angular velocity, R is blade radius, and v is wind speed.

The C_P - TSR curve identifies the optimal operating point for maximum efficiency. In the curve it is also represented an horizontal dashed red line at $C_P = 0.6$ that denotes the Betz limit: no turbine can exceed this efficiency limit due to physical constraints in energy extraction. Wind speed changes dynamically, and the rotor speed varies accordingly. The $C_P - TSR$ curve helps in predicting how the turbine performs across different wind speeds and rotor speeds, ensuring that the generator can handle variations without losing efficiency or overloading.

Figure 1.7: Curve C_P - TSR

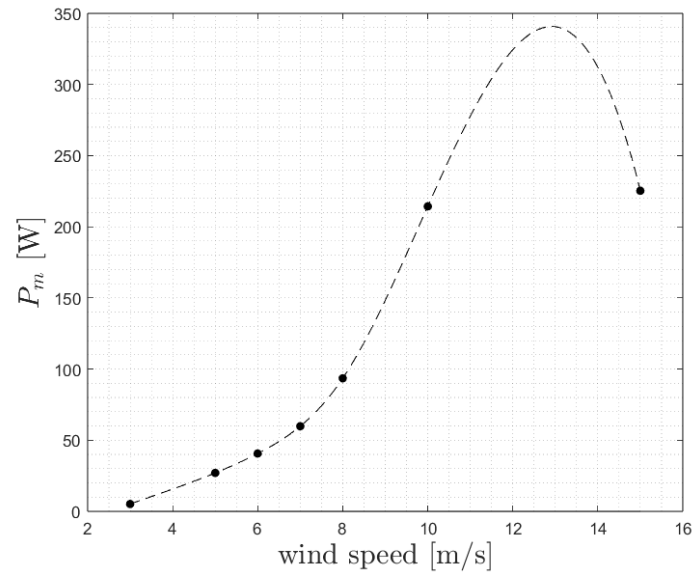
At $TSRs$ lower or higher than the optimal range, the power coefficient drops, meaning less energy is captured. A generator that doesn't match the rotor's dynamics could inadvertently operate the rotor in these less efficient regions.

The graph 1.8 is crucial in characterizing the performance of wind turbines under varying wind conditions. It helps engineers understand at which wind speeds the turbine performs optimally and where efficiency losses occur. It can be seen that the efficiency tends to drop at higher wind speeds (above 10 m/s), potentially due to aerodynamic losses, blade stalling.

Figure 1.8: Curve $C_P - V_{wind}$

Shown below the graph 1.9 of the mechanical power and the speed of the wind, which was hypothesized not to be above the 15 m/s , also for the strength of the rotor structure. The power equation:

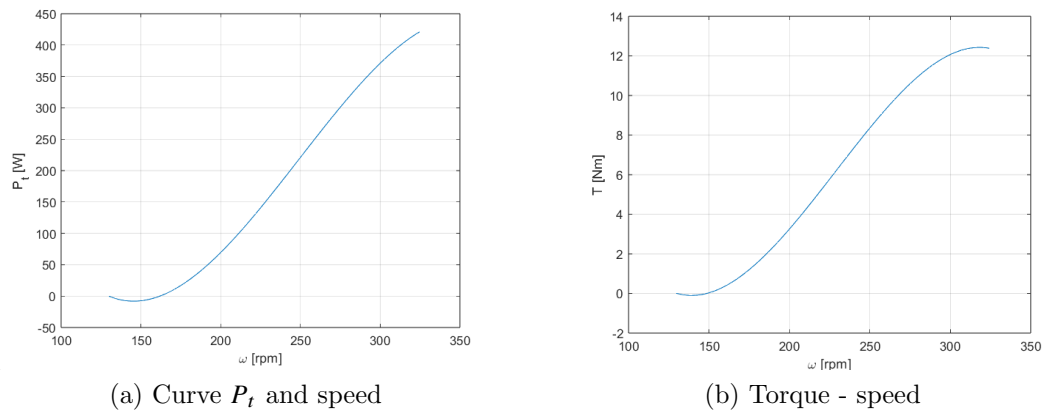
$$P_m = \frac{1}{2} \cdot \rho \cdot S \cdot v_{wind}^3 \quad (1.3)$$

Figure 1.9: Curve $P_m - V_{wind}$

The latter graphs (i.e. figures 1.10a and 1.10b) are the ones based on the size of the new generator: the curve of mechanical power and the speed rotor are necessary to start the sizing of the machine.

Where the rotor power is given by the formula:

$$P_t = C_P \cdot P_m \quad (1.4)$$

(a) Curve P_t and speed

(b) Torque - speed

Figure 1.10: Power and Torque requested

The rotor torque is given by the formula:

$$T = \frac{P_t}{\omega} \quad (1.5)$$

Chapter 2

Benchmarking of the Available Generator

In this chapter, benchmarking of the generator is performed, with the goal of identifying its performance limitations.

The geometric and dimensional data of the generator are analyzed, followed by constant speed tests to evaluate its efficiency. Experimental results, obtained through voltage and phase resistance measurements, reveal that the current generator suffers from high Joule losses and is unable to deliver the power required for the intended application.

Due to these problems, the chapter introduces the specifications for a new generator, laying the foundation for the design and optimization discussed in subsequent chapters. The analysis shows that the main weakness is the stator windings, suggesting that optimization of this component can significantly improve overall performance.

First of all, it has been studied the graph given by the manufacturer of the generator, reported in fig. 2.1.

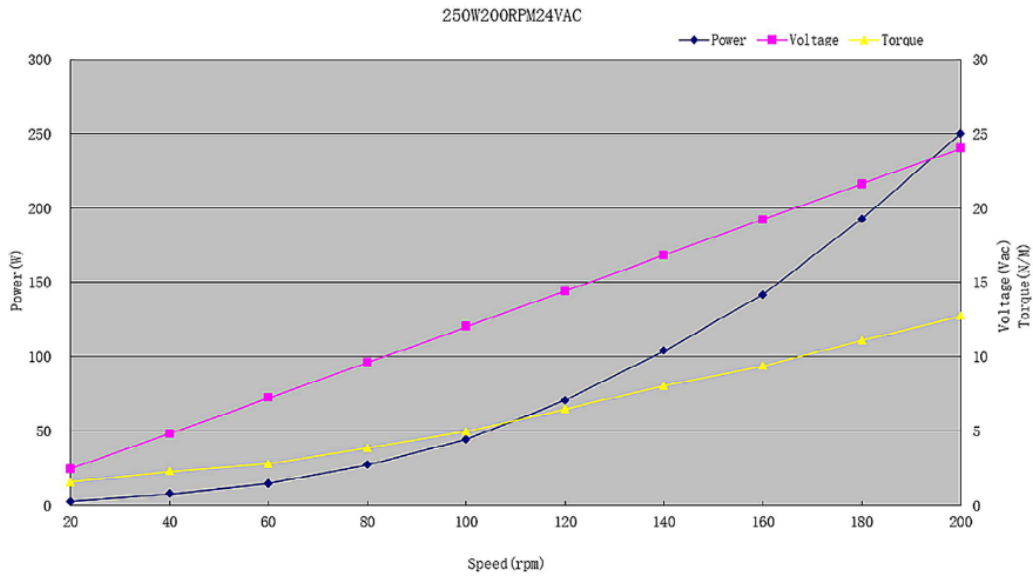


Figure 2.1: Curve Graph

The voltage shown in the graph is most likely the generator's open-circuit voltage, i.e., the electromotive force (EMF) during a no-load test.

In the absence of electrical load ($I \approx 0$), the terminal voltage coincides with the electromotive force.

From the graph, the voltage (pink line) increases linearly with speed ($V \propto n$), which is typical for a no-load test. In paragraph 2.1, it will be described the open-circuit test.

For the power, initially it was thought as the previous case that it could be a no-load test, no useful power is delivered since there is no electrical load. The measured power corresponds to the internal losses of the generator:

$$P_{\text{no-load}} = P_{\text{mech}} + P_{\text{magn}} \quad (2.1)$$

where:

- P_{mech} : mechanical losses (e.g., friction, ventilation).
- P_{magn} : magnetic losses (e.g., hysteresis, eddy currents).

In this case, moreover, since it is a coreless motor — so no iron core — and operates within a low-frequency range, magnetic losses due to eddy currents and hysteresis are by definition almost negligible compared to mechanical losses, it could not be a test at no load.

This power is typically very low at low speeds and increases with speed, as both mechanical and magnetic losses grow with rotational speed. The reported power (blue line) increases slowly at low speeds and rises progressively at higher speeds, but the power values shown are very high for mechanical losses. So, this behavior does not align with a no-load test, where power is only due to internal losses.

So, assuming that the depicted voltage is indeed the no-load voltage, the depicted power appears to be simply a theoretical electrical power based on the no-load voltage, meaning the power available if the generator had no internal losses, i.e., with zero winding resistance.

For the torque, the same considerations applies.

The torque (yellow line) is low at low speeds and grows moderately with speed, proportional to the power. The equation is:

$$T = \frac{P_{electromagnetic}}{\omega} \quad (2.2)$$

where $P_{electromagnetic}$ is the power calculated with the sizing equation of the generator.

Based on the graph, only the voltage appear to be measured under no-load conditions, because the voltage increases linearly with speed, consistent with open-circuit EMF.

So, as a first analysis, considering the observations on the datasheet graph, it is important to characterize the motor by performing a no-load test, measuring the generator's resistance to evaluate Joule losses, and finally conducting a load test.

These observations will be validated in the next paragraph with analytical calculation.

2.1 Generator Benchmarking and Analysis

The objective of testing this generator is to gather as much information as possible to optimize its design according to the required specifications. A key focus is to determine the geometry of the winding turns to better understand the magnetic path, identify potential sources of major losses, and pinpoint the parameters that need to be optimized.

2.1.1 Geometric Data and Dimensions

First of all, the dimensions of the rotors and the stator are provided. The measurements of non-magnetic parts are taken using a caliper. Obviously the measurements were fundamental to study the generator parts and for the optimization of its.

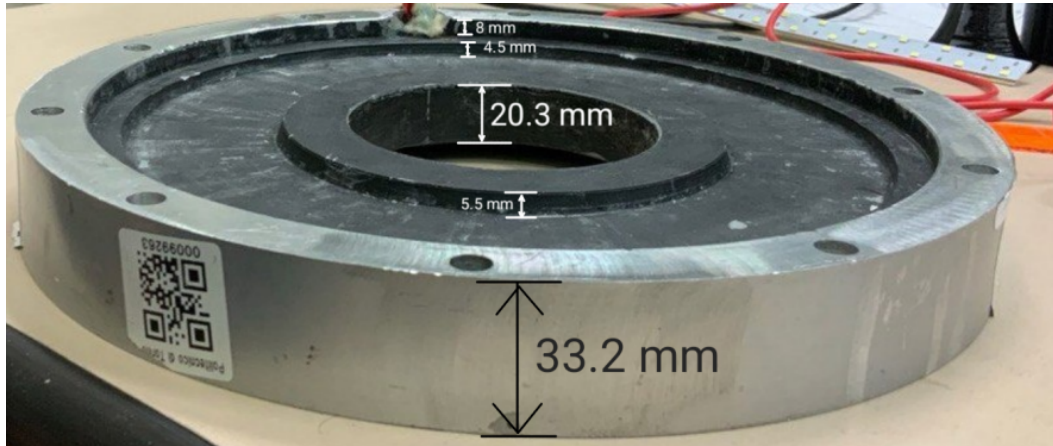


Figure 2.2: Geometric dimension of the stator



Figure 2.3: Geometric dimension of the stator

For the rotor and the magnets it has been used a plastic caliper. The two rotors present both some markings on the protective coating of the magnets, likely caused by mechanical stresses during the utilization of the generator.

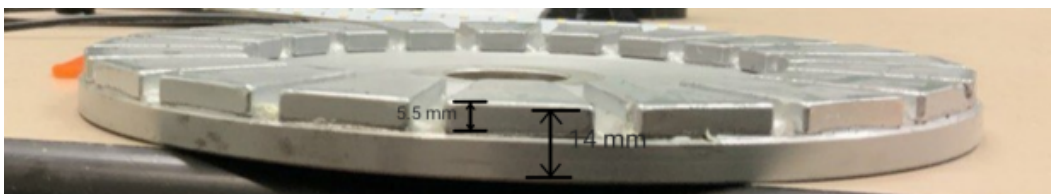


Figure 2.4: Geometric dimension of the rotor



Figure 2.5: Geometric dimension of the rotor

Back EMF, Resistance and Flux

The first selected tests for this motor are aimed at obtaining the previously mentioned data, which will be derived from the following formula:

$$E = \frac{2 \cdot \pi}{\sqrt{2}} \cdot f \cdot \lambda \quad (2.3)$$

where $f = \frac{\omega}{2\pi}$ is the frequency, N is the number of turns in series per phase, $\lambda = \phi_m \cdot k_w \cdot N$ is the linkage flux, ϕ_m is the magnetic flux of magnet and k_w is the winding factor that is given by the product $k_p \cdot k_d$, where k_p is the pitch factor and the k_d is the distribution factor, these factors depend exclusively on the geometry of the windings. With this formula it can be obtained the N number of turns.

The first test conducted on this generator was for the magnetic flux of the magnets (Φ_m) and the winding resistance (R).



Figure 2.6: Test Bench

This test was conducted by the members of Team EoliTo from Politecnico di Torino to determine the magnetic flux of a permanent magnet synchronous generator. The methodology was based on voltage measurements taken from one phase of the generator, with the flux calculated as the time integral of the measured voltage.

All evaluations were performed numerically using MATLAB.

The experimental setup was carried out in the Enertronics Laboratory of the Department of Energy (DENERG).

The measurement setup involved connecting the generator to a Tektronix benchtop power supply, a benchtop multimeter, and a Fluke portable multimeter. The data were recorded using an HBM high-speed acquisition system capable of handling differential channels with a peak voltage of ± 1000 V, real-time star voltage calculations, and a sampling resolution of 500 ns. The acquired data were then processed in MATLAB using HBM-provided software, which converted the raw acquisition data into numerical vectors for analysis. Before proceeding with the flux measurement, the winding resistances of the generator were determined. A current of 1 A, equivalent to $\approx 17\%$ of the nominal 6 A, was injected into the generator's phases to minimize Joule losses

and avoid significant temperature variations. The measurements were carried out for three phase pairs (1-2, 2-3, and 3-1), and the results were consistent, with a measured resistance of $1.672\ \Omega$.

Phase measurement	Voltage [V]	Current [A]
1-2	1.672	0.999
2-3	1.671	0.999
3-1	1.673	0.999

Table 2.1: Resistance measurement of a winding.

The value of phase resistance is very high. Unfortunately, since it is not possible to know the cable's cross-section or the winding material, it is not possible to determine whether such a high resistance value is due to a material with poor electrical conductivity or to damage sustained by the generator during use either it could also simply be the high number of coils in series per phase. As mentioned earlier, the stator consists only of windings and this layer of insulating material that keeps the windings attached. Taking this layer into account, not knowing the thickness of either the windings or the insulation or even the number of layers, it is difficult to speculate on the nature of the windings: what cross section is used or what material is used to wind this stator. Conclusions and further assumptions will be made in the last chapter.

In the figure 2.7, it can be seen the joule losses are very high, due to the high resistance measured, until reaching $60W$, a huge value for such a small generator.

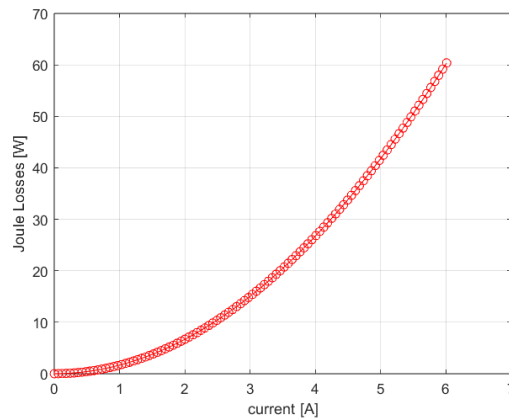


Figure 2.7: Joule Losses

The flux measurement involved high-speed voltage acquisition across the generator's three phases. The phases were numbered; depending on how the generator is rotated, the sequence changes. The star center has the property of rejecting third harmonics (multiples of three). Therefore, a star center was created in the acquisition system, resulting in phase electromotive forces where third harmonics are absent compared to the true phase electromotive forces.

The generator was rotated (in the clockwise direction, which was associated with the positive sequence convention) to obtain phase voltages that vary both in amplitude and period. The integral of these voltages is constant over time and represents the flux linkage: only the flux of the magnets in the windings is present, as long as no current is injected.

The flux was then calculated by integrating the phase voltage over time. Integration drift was mitigated by defining hysteresis levels, ensuring reliable results. Once the data were processed, the sinusoidal flux components (α and β) were reconstructed using the Space Vector Inverse Transformation method. The flux linkage was calculated as the root sum square of the α and β components, resulting in a final value of

$$\lambda = 111.9 \text{ mVs} \quad (2.4)$$

As mentioned in the beginning of the paragraph 2, it was also performed to provide evidence that these voltage values were associated with the open-circuit test. All measurements were carried out under the assumption that the generator operates with a balanced three-phase system.

Speed [rpm]	$E_{peak \text{ measured}}$	$V_{phase, rms, from \text{ graph}}$	$V_{phase, peak, from \text{ graph}}$
80	$\approx 5.7 \text{ V}$	$\approx 9.5 \text{ V}$	≈ 5.5
160	$\approx 11.1 \text{ V}$	$\approx 19 \text{ V}$	$\approx 11 \text{ V}$
200	$\approx 13.5 \text{ V}$	24 V	$\approx 13.9 \text{ V}$

Table 2.2: Results of EMF-test

Where it is stated that $V_{phase} = E$, and the graph is referring to the one 2.1.

An ammeter was also connected to the generator terminals during the test. The current was effectively zero, that confirms the generator was operating under no-load conditions.

Clearly, these data are not sufficient to calculate the exact number of turns. However, it is possible to calculate the equivalent number of turns:

$$N_s^* = N_s \cdot k_p \cdot k_d \quad (2.5)$$

where k_p being the pitch factor and k_d the distribution factor, with the help of the formulas seen in [8].

The magnetic flux and the number of turns per pole were calculated analytically. Below are reported the equation and the results.

$$\phi_{mg} = \alpha_i \cdot B_{mg} \cdot \frac{\pi}{pp} \cdot (R_{ext}^2 - R_{int}^2) = 1.0246 \text{ mVs} \quad (2.6)$$

where α_i is the ratio of the magnet width to the polar pitch, B_{mg} is the magnet induction.

$$N_s^* = \frac{E}{\frac{2 \cdot \pi}{\sqrt{2}} \cdot f \cdot \phi_{mg}} = 90 \quad (2.7)$$

In fact, to obtain further confirmation, multiplying the magnetic flux for the number of turns obtained actually finds the measured flux linkage.

Thermographic camera test

To gather the necessary information about the windings, it would have been ideal to split the stator in half to count the number of turns and slots, measure their dimensions, etc. However, since the generator belongs to the EoliTO team, this approach was not feasible, so an alternative method was used.

The solution involved heating the generator by applying a DC voltage (with two phases connected in parallel) until the motor reached a temperature necessary to see the windings, under the manufacturer's specified limits. By supplying 5 A and 5.9 V, the winding layout became visible using a thermal imaging camera.

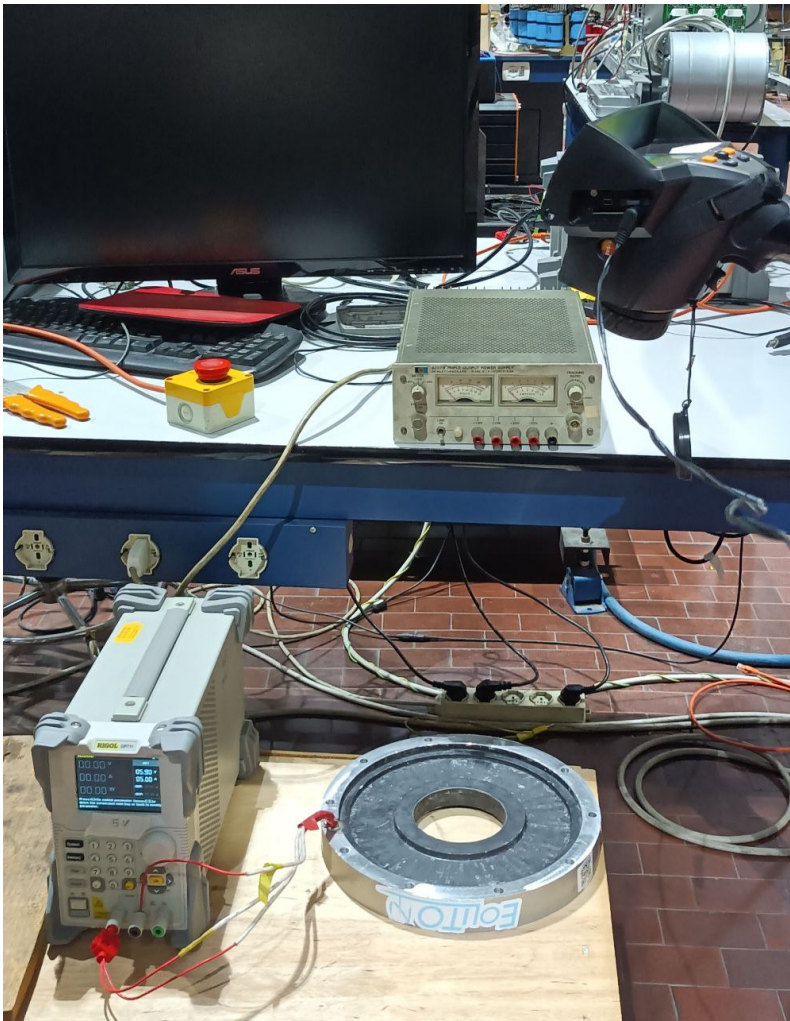


Figure 2.8: Test setup with the supply



Figure 2.9: Test setup with thermographic camera

The images captured by the thermal camera confirmed that the generator was wound with concentric windings, as previously assumed. Additionally, from the resulting images (see figs. 2.10 and 2.11), the closures of certain windings were not visible, suggesting the possibility of double-layer winding. For this reason, the stator was examined from both sides. Indeed, it appears that each winding loops back into the one below, as observed in Figures 2.10 and 2.11. Using the external reference point (i.e. the red figure outside the stator) as an indicator for the start and end of the coil, this pattern becomes evident.

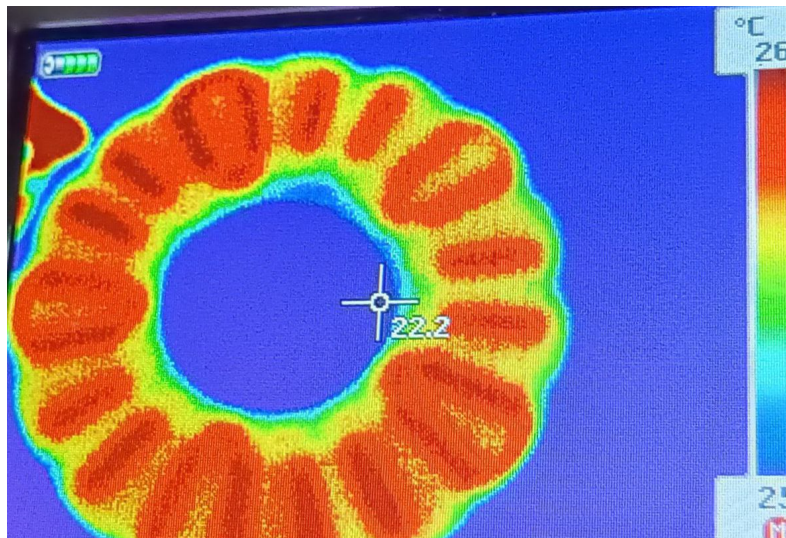


Figure 2.10: One side of the stator

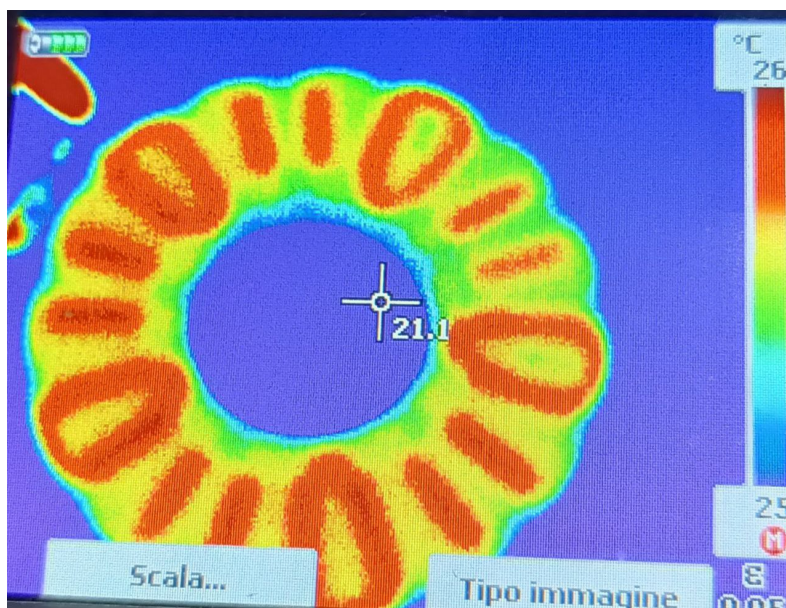


Figure 2.11: The other side of the stator

This test was conducted to try to understand at least the type of winding and whether it was single or double layer.

Now that it is known that the winding is concentric and double-layered, it is possible to apply the sizing equations given from [8], in order to confirm the hypothesis made at the begin of the chapter.

The relative permeability of the magnet is given by:

$$\mu_{r_{rec}} = 1 + \frac{B_r}{H_{cj}} \quad (2.8)$$

where:

- B_r is the remanent flux density of the magnet,
- H_{cj} is the coercive field strength.

The effective airgap is calculated as:

$$g = \frac{t - t_w}{2} \quad (2.9)$$

The flux density in the airgap is given by:

$$B_{mg} = \frac{B_r}{1 + \left(\mu_{r_{rec}} \frac{g + t_w/2}{l_m} \right)} \quad (2.10)$$

For a double-layer winding, the number of slots and coils per phase is:

$$s_1 = 20, \quad n_c = \frac{s_1}{m_1} \quad (2.11)$$

The number of turns per coil is:

$$N_{tc} = \frac{N}{n_c} \quad (2.12)$$

The coil side per pole per phase is:

$$q_1 = \frac{s_1}{ppm_1} \quad (2.13)$$

The coil span in coil sides is:

$$\tau_c = \frac{s_1}{pp} \quad (2.14)$$

The winding distribution factor is given by:

$$k_d = \frac{\sin\left(\frac{\pi}{2m_1}\right)}{q_1 \sin\left(\frac{\pi}{2m_1 q_1}\right)} \quad (2.15)$$

The number of revolutions per minute is:

$$n = 200 \quad (2.16)$$

The back electromotive force constant is:

$$k_e = \frac{\pi\sqrt{2}pp}{2}N\phi_{mg} \quad (2.17)$$

The rotational speed in Hz is:

$$n_{sec} = \frac{n}{60} \quad (2.18)$$

The torque constant is:

$$k_t = \frac{k_e m_1}{2\pi} \quad (2.19)$$

The induced electromotive force is:

$$EMF = k_e n_{sec} = 13.8V \quad (2.20)$$

The developed torque is:

$$T_d = k_t I_{ph} \approx 12 Nm \quad (2.21)$$

Finally, the electrical power is:

$$P_{elm} = n_{sec} T_d 2\pi \approx 250W \quad (2.22)$$

All data match the specifications given by the manufacturer.

2.1.2 Test at Constant Motor Speed

Through this test, it is intended to verify how the generator actually suffers from the Joule losses that penalize the total efficiency, but also that it can not support 350 rpm.

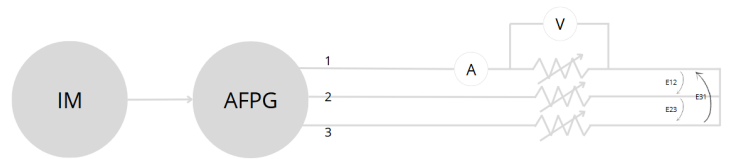


Figure 2.12: Generic schematic of the test

The test is introduced by explaining the test bench: the prime mover, an asynchronous motor, induces rotation in the AFPM generator through a toothed belt, with its rotation speed controlled by an inverter. Between the generator and the load, represented by the variable resistance, there is the data acquisition system developed by Team EoliTo, which consists of a rectifier with a diode bridge, a current sensor circuit with a shunt resistor, and a voltage sensor.

The test was carried out by keeping the speed constant (through the inverter connected to the prime mover) while increasing the load on the AFPM generator by increasing the load resistance value.

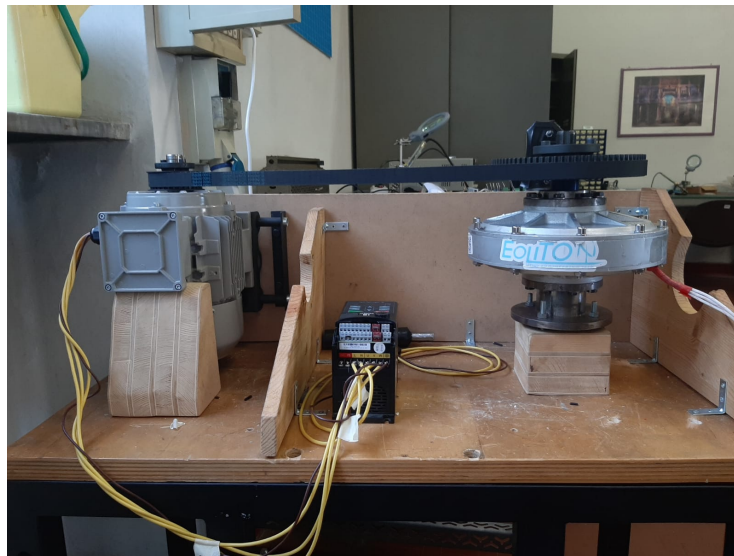
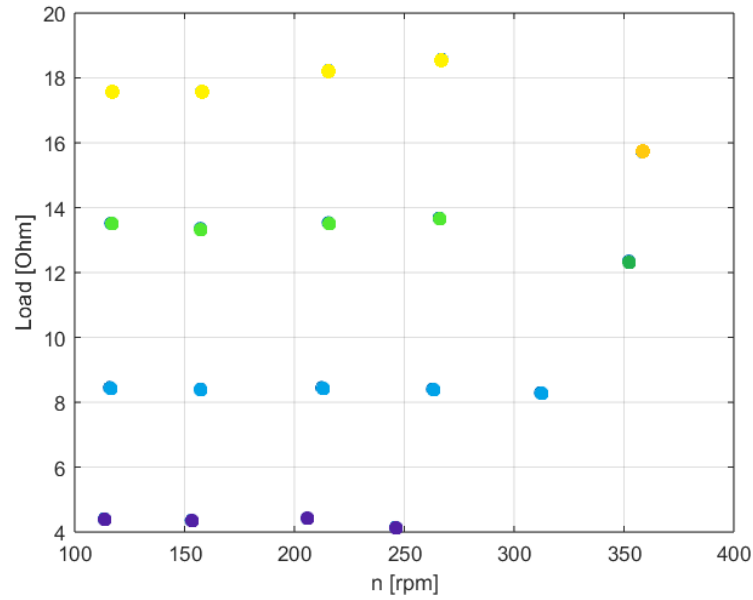


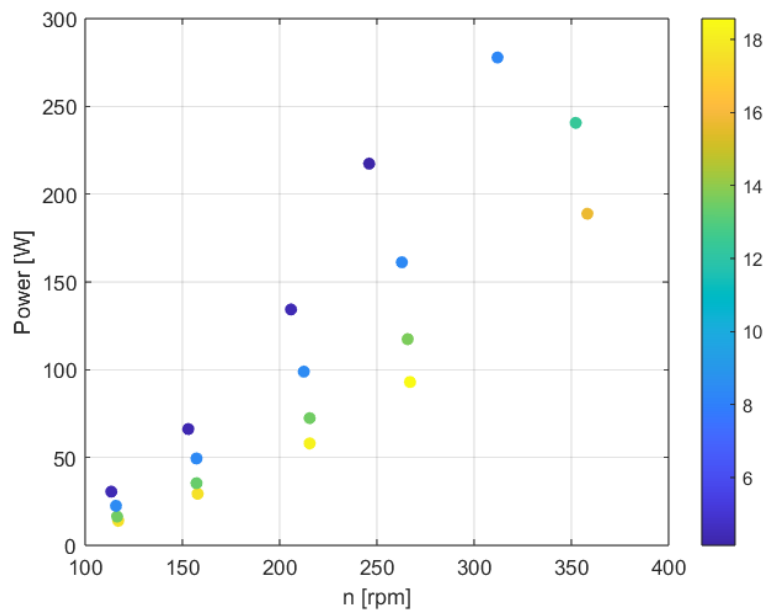
Figure 2.13: Bench of the load test

The graphs 2.14a and 2.14b should be analyzed together. The colors are used to clearly show that each resistive load corresponds to its respective power, marked by a dot of the same color. As expected, the generator delivers less power than the theoretical value due to losses. By observing both graphs

together, it becomes evident that Joule losses are by no means negligible, making this parameter undoubtedly worth optimizing.



(a)



(b)

Figure 2.14: a) load and speed measured; b) Power and speed - color scale: the load range in resistance [Ω]

The resistance in graph 2.14a represents the rheostat resistance used to simulate the load. The test was conducted at a fixed speed while increasing

the load to determine the power output for each imposed speed. As evident from the graph, the generator was actually pushed beyond the speed limit specified in the datasheet. In fact, with a low load, the system successfully sustained the test, and the results were consistent, whereas at higher loads and speed, the generator was unable to generate the required power, and the vibrations were extremely high.

As it was expected, the generator suffer with evidence of Joule losses, as the calculation predicted. More the load increases, more the generator suffer and it has not being able to generate sufficient power and torque, and obviously less that declared in the graph 2.1.

2.2 Benchmarking Results and Comments

Benchmarking data confirms the assumption. The nameplate data are confirmed as assumed in the previous chapter: the voltage represented is the no-load voltage, the power and torque are the parameters found with the sizing equation, obtained also with the sizing equation known from the thesis [8] as can be seen in section 2.1.1.

The AFPM generator has many advantages, first of all the absence of iron in the core is a great savings in terms of material and also of losses. In this case, however, the generator does not have the sufficient generation of power needed for the application and does not withstand the speed that the rotor could hypothetically endure. It could be seen in the test at constant speed: as soon as the load increases or the speed increases the generator began to experience mechanical vibrations harmful to the system, causing a significant power losses. The target initially proposed, it is not achieved, above all due to the joule losses. Measuring the phase resistance was fundamental to understand the cause of the majority of the losses. Also studying the type of windings it was at least possible to determine the number of coil groups and also to understand the geometry of the windings.

In conclusion, it starts from the fact that the generator is not designed to sustain the speeds required in the first chapter, neither it can generate the required power.

The target is to create a generator that produces sufficient power and potentially has lower Joule losses. The decision was made to optimize the stator

windings because, based on the analyses so far, they are the weak point of the generator, but also the most cost-effective element to optimize. The goal is to have an optimized generator, keeping the beneficial aspects of the structure and reshaping those elements that cause efficiency losses.

2.3 New Generator Specs

Through the graph 1.9, 1.10a, some considerations have been made before starting to size the new generator.

The data were chosen as follows:

- **Voltage:** The voltage was selected based on the components already existing within the team. The inverter to which the generator is then connected supports 24V. The phase voltage was calculated by dividing the line voltage by the square root of three.
- **Current:** The current was derived from the power equation, assuming a unitary power factor:

$$P = \sqrt{3} \cdot V_{\text{phase}} \cdot I_{\text{phase}} \quad (2.23)$$

- **Frequency:** The frequency was calculated using the formula:

$$f = \frac{\text{rpm} \cdot 2p}{120} \quad (2.24)$$

- **Speed & Power:** Speed and power were selected based on the specifications provided by the Eolito team.

Parameters	Value	Unit
<i>Power</i>	350	W
<i>Speed</i>	350	rpm
<i>V_{phase}</i>	13.86	V
<i>Frequency</i>	58.33	Hz
<i>I_{phase}</i>	8.42	A
<i>Pole pair</i>	10	

Table 2.3: Main parameters

The dimensions of the previous stator are referenced, as the two structures of the pre-existing rotor are maintained. The main parameters are summary below.

Parameters	Value	Unit
R_{ext}	104	mm
R_{in}	15	mm

Table 2.4: Parameters of the rotor

Parameters	Value	Unit
Axial Thickness	5.5	mm
Axial Height	15	mm
External radial thickness	25.5	mm
Internal radial thickness	17.5	mm
Radial Height	37	mm

Table 2.5: Parameters of the magnets

It was decided to maintain the rotor structure, thanks to the excellent qualities of the magnets and their good condition and optimize the stator. Retaining the rotor is not only a choice driven by the good condition of the magnets but also a budget-related decision. One of the key goals of the project is to keep costs as low as possible.

Chapter 3

Design of the New Generator

As previously mentioned, the two rotors have been retained, since they appear to be in good condition and are therefore considered unchanged in this analysis to reduce production costs.

In the following analysis, two design paths will be explored: the PCB stator and the coreless stator.

This chapter aims to compare the similarities and differences between these two stator technologies, focusing on their design principles, technological aspects, and performance metrics.

Starting from the similarities, both PCB and coreless stators are designed to minimize iron losses, a significant factor in improving the overall efficiency of AFPMSGs. The similarities between the two technologies include also:

- **Ironless Structure:** Both designs avoid the use of ferromagnetic cores, eliminating hysteresis and eddy current losses.
- **Compact Design:** PCB and coreless stators enable a reduction in weight and volume, making them suitable for applications where space constraints are critical.
- **Thermal Management:** Both stator types can incorporate thermal management techniques.

The performance of PCB and coreless stators can vary significantly depending on the specific application and operating conditions. Key performance metrics include efficiency, power density, and thermal stability.

The PCB stator benefits from its precise manufacturing process, allowing for

optimized conductor layouts. However, the coreless stator can achieve higher efficiency in applications requiring low-speed operation due to reduced eddy current effects.

Coreless stators typically achieve higher power densities compared to PCB stators, primarily due to their ability to accommodate thicker windings and higher current capacities. Conversely, PCB stators are often limited by the thickness of the PCB substrate.

While PCB stators offer improved thermal dissipation due to the inherent properties of the PCB material, coreless stators may require additional cooling mechanisms to manage heat generated during high-power operations.

Despite the similarities, several critical differences differentiate PCB and coreless stators:

- **Manufacturing Complexity:** PCB stators exploit established PCB manufacturing processes, resulting in high precision and repeatability. Coreless stators, on the other hand, often require custom winding techniques, which can increase manufacturing complexity and cost.
- **Mechanical Rigidity:** The PCB stator exhibits higher mechanical rigidity, which can be advantageous in high-vibration environments. In contrast, the coreless stator flexibility may limit its mechanical robustness.
- **Scalability:** PCB stators are more scalable due to their modular design, while coreless stators are often tailored to specific applications, limiting their adaptability.

While PCB and coreless stators share common advantages, such as reduced iron losses and compact designs, their performance diverges in specific areas such as power density, efficiency, and thermal management. The choice between these two technologies depends on the intended application, operational requirements, and cost considerations.

At the conclusion of this study, a design choice will be made.

In the next paragraphs, these two types of stators will be compared through a preliminary analysis, focusing on the study of windings in the case of coreless stator and traces in the case of PCB stator.

3.1 Coreless Stator Sizing

The previous stator was coreless and slot-less. The windings are suspended in a black insulating material, which holds them fixed. In the hypothesis of optimizing the generator by rewinding it, the use of a slot-less design would be maintained.

In addition to the absence of a ferromagnetic core in the stator, which limits the concentration of the magnetic flux and reduces the achievable flux density in the air-gap, the lack of slots can result in a lower torque density compared to motors with slots. This often requires the use of more powerful magnets or larger dimensions to achieve comparable torque.

Since the windings are distributed without the aid of slots, a higher amount of copper is required to achieve the same current density as a motor with slots. This also increases the material cost.

The winding configuration was created using Dolomites[10]. In the fig. 3.1, it can be seen the number of slots (Q), number of pole ($2p$), the winding factor (k_w), t is the GCD(Q , p) that is the periodicity of the machine, given by the greater common divisor (GCD) between Q and p , the number of coils per group (N_{cpg}), that in this specific case is an integer, given by the formula

$$N_{cpg} = \frac{Q}{m|Q - 2p|} \quad (3.1)$$

and the coil throw (yq) is expressed in number of slots and defined as the integer closest to the ratio between the number of slots and the number of poles, i.e.,

$$yq = \text{round}(Q/2p) \quad (3.2)$$

In this specific case, $t = 2$, which means that the machine has a periodicity of 2, implying that the winding layout and the magnetic field pattern repeat every two units.

Three phase winding wizard

Slots Q

Select range from 3 to 24

Q divisible by: 6

Coil throw yq

Choose yq 1

Single layer feasible

No mutual coupling

Poles 2p

Select range from 20 to 20

Winding factor Kw

Select range from 0.00 to 1.00

Equal groups

Equal groups of coils ON

Number of coils per group 0

1 items Search winding

	Q	2p	kw	t	\hat{N}_{cpg}	yq
1	24	20	0.933013	2	2	1

OK Cancel

Figure 3.1: Winding with Dolomites

Finally, the increased reluctance due to the absence of a ferromagnetic core can affect the motor efficiency, although this is usually compensated by optimizing the magnet and the winding geometry, as said in previous chapters.

A stator with non-overlapping, double-layer windings was chosen. First, it is necessary to set some boundaries [10] for poles and slot combinations in non-overlapping windings:

- the number of poles must be even,

- the number of slots must be a multiple of the number of phases,
- the number of coils in a group must be an integer,
- the number of slots cannot be equal to the number of poles,
- the number of coils and slots are equal in double layer windings, while in single layer windings the number of coils is equal to half the number of slots.

With the help of Dolomites, a winding was created with the characteristics previously mentioned, and without mutual inductances, thus resulting in an optimized winding configuration.

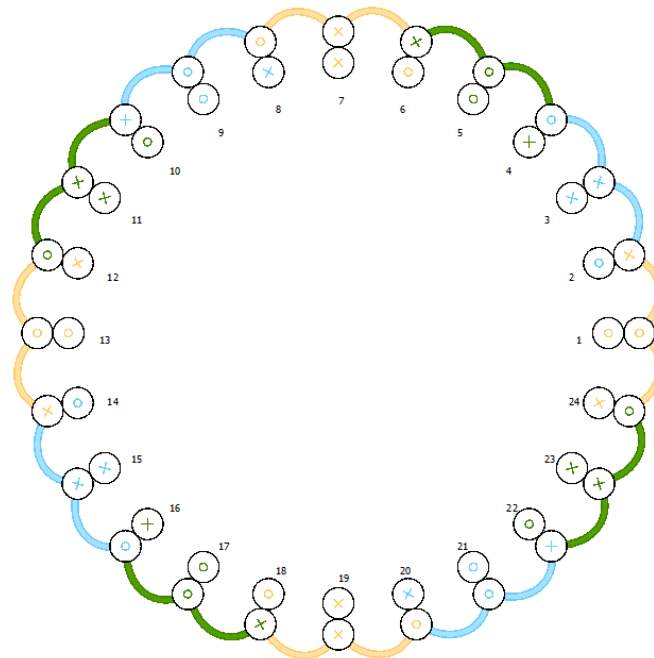


Figure 3.2: Coreless stator winding

Parameter	Value	Unit
Airgap	10	mm
N° slot ¹	24	
N° turns in series per phase	90	
N° of coil side per pole per phase	2/5	
Thickness Coils	8	mm

¹By software definition, the term “slot” is used, but in the specific case of this technology, it does not actually refer to physical slots. Instead, it refers to “figurative” slots, which do not physically exist but theoretically indicate the spatial distribution of the windings.

As in the previous generator, the number of turns are 90, but the number of slot are 24, instead of 20.

3.1.1 Sizing equation

From the master thesis [8], it has been sized the coreless generator.

First, the number of coils per phase for a double layer windings, as designed in Dolomites, was established by the formula:

$$n_c = \frac{s_1}{m_1} \quad (3.3)$$

where s_1 is the number of slots and m_1 is the number of phases.

The number of turns per coil is calculated as:

$$N_{ct} = \frac{N_1}{n_c} \quad (3.4)$$

Where N_1 is the number of turns in series per phases and it is calculated with the inverse of the EMF formula 2.7.

The number of coil sides per pole per phase is given by:

$$q_1 = \frac{s_1}{2p \cdot m_1} \quad (3.5)$$

The air gap is half the difference between the total air gap thickness and the winding thickness:

$$g = \frac{(t - t_w)}{2} \quad (3.6)$$

The pole pitch, measured in coil sides, is determined by:

$$\tau_c = \frac{s_1}{2p} \quad (3.7)$$

Focusing on the magnetic aspects of the motor, the air-gap magnetic flux density produced by permanent magnets is computed as:

$$B_{mg} = \frac{B_r}{1 + \left[\mu_{rrec} \left(\frac{g+t_w/2}{h_M} \right) \right] k_{sat}} \quad (3.8)$$

where B_r is the residue magnetic field, k_{sat} is the saturation factor that is supposed equal to 1, μ_{rrec} is the dimensionless permeability of the N42H magnets,

and it is given by the formula:

$$\mu_{rec} = 1 + \frac{B_r}{H_{cJ}} \quad (3.9)$$

where H_{cJ} is the intrinsic coercivity.

The magnetic flux is given by:

$$\phi_f = \alpha_i B_{mg} \pi \frac{1}{2p} \left[\left(\frac{D_{out}}{2} \right)^2 - \left(\frac{D_{in}}{2} \right)^2 \right] \quad (3.10)$$

where the α_i in this specific case is the ratio between the magnet width and the pole pitch

$$\alpha_i = \frac{s_{mg}}{\tau} \quad (3.11)$$

Another key factor impacting on the generator performance is the winding factor, which is the product of the distribution factor and the pitch factor:

$$k_{w1} = k_{d1} \cdot k_{p1} \quad (3.12)$$

Where the distribution factor k_{d1} is defined as:

$$k_{d1} = \sin \left(\frac{\pi}{2m_1} \right) / q_1 \sin \left[\frac{\pi}{2m_1 q_1} \right] \quad (3.13)$$

Since the winding factor was obtained using the Dolomites software, the pitch factor is derived with the inverse formula of k_{w1} .

The EMF constant:

$$k_E = \pi \sqrt{2} p N_1 k_{w1} \phi_f \quad (3.14)$$

The torque constant:

$$k_T = k_E \frac{m_1}{2\pi} \quad (3.15)$$

The EMF at the given speed:

$$E_f = k_E n \quad (3.16)$$

Given these constants and the parameters, which will be optimized subsequently, the electromagnetic torque and power values can be calculated.

Electromagnetic torque:

$$T_d = k_T I_a \approx 15 \text{ Nm} \quad (3.17)$$

And finally the electromagnetic power:

$$P_{elm} = 2\pi nT_d \approx 560 \text{ W} \quad (3.18)$$

By keeping the dimensions of the previous generator unchanged, the magnetic flux and the linkage flux are preserved.

Finally, to compare the Joule losses, the total resistance of the windings was calculated as follows[5], considering at room temperature.

$$R_f = \rho_{cu} \cdot \frac{L_{tf}}{S_{cu}} \quad (3.19)$$

Where

$$\rho_{cu}(T) = 1.76 \cdot 10^{-8} (1 + 0.0039(T - 20)) \quad (3.20)$$

and

$$L_{tf} = L_{sp} \cdot N \quad (3.21)$$

$$L_{sp} = 2 \cdot [(R_{ext} - R_{int}) + A_{zs}] \quad (3.22)$$

where L_{tf} is the total length of the turns in series, L_{sp} is the length of the turns, A_{zs} is the axial thickness of the stator core and S_{cu} is the cross-section of the conductor that makes up the coil.

Since the dimensions of the stator were kept the same in both cases (see the PCB stator dimensions later), the magnetic path of the windings was sized using the dimensions taken from the generator studied so far. As for the choice of the conductor thickness that constitutes the coil, unfortunately, it was not possible to rely on the previous generator since it could not be disassembled for verification. Therefore, knowing that for powers below 10 kW it can be assumed that the current density is $6 - 7 \text{ A/mm}^2$, a copper cross-sectional area of 1.5 mm^2 was hypothesized. It has been considered all the turns in series per phase. The phase resistance at 20° C is

$$R_f = 0.2 \Omega \quad (3.23)$$

3.2 PCB Stator Sizing

Selecting the PCB stator clearly has advantages and disadvantages.

- Usually the cost is lower compared to rewinding a generator. Although an exact estimate is unavailable, it is well known its low cost, especially for a double-sided (not multilayer) PCB, considering it is for a small-scale generator, compared to the cost required for an iron-less stator[9].
- It allows for a reduced air-gap compared to the coreless solution, potentially achieving a better trade-off between reluctance and inductance. Although the coreless generator also features a double-layer design, as in the case of the PCB structure, in this case, the thickness of the PCB is much smaller compared to the structure made of insulating material used to fix the windings.
- One advantage of using a PCB is the ease of integration with power electronics. This opens the possibility of embedding a current sensor and a position sensor directly onto the PCB for real-time data acquisition.
- A probable reduction in torque and lower induced voltage under the same conditions as the coreless solution, which likely implies a greater use of copper.

The parameters that have to be analyzed:

- A relatively high *resistance* is to be expected, primarily due to the geometry of the PCB traces. Copper traces typically have a limited cross-sectional area (reduced width and thickness compared to conventional conductors), which increases the conductor's resistance.
- *Inductance* will mainly depend on the geometric configuration of the windings and the presence of a magnetic core. On a PCB, with flat traces and reduced distance between conductors, the inductance may be lower compared to coils made with multi-layered wound copper wire. However, it can become significant if the magnetic path is long or if the number of turns is high.

Furthermore, inductance limits the rate at which current can change in response to voltage variations. When the generator supplies power to a

load, the inductance dampens sudden current fluctuations. Given the relationship $\tau = \frac{L}{R}$, where L is the circuit inductance and R is the circuit resistance, it is clear that a higher inductance results in a larger time constant, indicating a slower response to rapid changes. Therefore, it is crucial for the inductance to have a low value to ensure the stability of the generator and to protect its components from sudden variations or undesirable oscillations.

- *Trace length* is the main factor determining electrical resistance. The resistance is proportional to the length according to the following equation:

$$R = \rho \frac{\text{trace length}}{\text{trace width} \cdot \text{trace height}} \quad (3.24)$$

- As the *trace width* increases, the resistance decreases due to the increased cross-sectional area. A reduced width can rapidly increase the resistance, leading to higher resistive losses.

Another matter element is the compact geometry, important for several reasons:

- *Reduction of resistive losses*: A shorter trace path reduces the electrical resistance.
- *Reduction of magnetic reluctance*: Reluctance (the magnetic equivalent of resistance) is influenced by the length and area of the flux path. A compact layout ensures the magnetic flux travels the shortest path with minimal losses.
- *Reduction of disturbances*: Closer turns reduce unwanted electromagnetic interference, increasing system efficiency.

Copper thickness is typically expressed in ounces per square foot (oz/ft^2) or in micrometers (μm). Below is a table of standard values:

Width oz/ft^2	Width μm
0.5	17
1	35
2	70
3	105
4	140
6	210

A great challenge in designing PCB-based AF-PMSMs lies in the PCB winding topology, which significantly impacts the electromotive force (EMF) and, consequently, the electromagnetic torque generated by the machine. The main type [2]:

1. *Concentric Windings*: it can take forms such as trapezoidal, rhomboidal, or spiral. The concentric windings aim to emulate the conventional windings of an AFPMSM. However, replicating the high number of turns typical of classical windings on a PCB is challenging. While multiple layers are possible, they can escalate costs quickly.
 - Trapezoidal windings exhibit a significant induced voltage and torque due to their extensive flux-linking area and elongated radial winding paths. However, their drawback lies in the surplus copper used in the tangential direction, which contributes no additional torque. Moreover, mechanical design constraints necessitate specific connection points for the copper traces, further increasing the copper length and resistance, leading to elevated power losses and heat generation.
 - The rhomboidal variant reduces copper length compared to the trapezoidal design but compromises torque due to partial misalignment with the radial direction, resulting in reduced resistance. Wave or distributed winding topologies are another common option, aimed at enhancing efficiency while maintaining the motor's dynamic performance. Tokgöz et al. [11] introduce four wave winding designs and compare their performance to identify their respective benefits.
2. *Parallel Windings*: These windings prioritize the shortest path to form a loop. Tokgöz et al. indicate that parallel windings reduce the total copper resistance to 74% compared to concentric windings. However, due to a smaller flux-linking area and suboptimal alignment with the radial direction, they result in lower induced voltage and torque.
3. *Radial Windings*: This design includes sections aligned with the radial direction, offering 33% greater torque than parallel windings. Additionally, radial windings exhibit higher induced voltage. However, since the

copper traces do not follow the shortest path, their resistance is slightly higher compared to parallel windings.

4. *Arc Windings*: Arc windings produce a more sinusoidal voltage waveform but have higher resistance due to an increased path length. Salim et al. [12] propose and test an arc winding design. Under sinusoidal current application, this design delivers smoother output torque compared to other types.
5. *Unequal Width Parallel Windings*: In certain configurations, the tracks are spaced farther apart near the outer edges of the PCB. This additional space can be utilized by widening the paths as they extend from the center, reducing phase resistance and improving power efficiency and thermal characteristics. Tokgöz et al. [11] explore this technique applied to standard parallel windings.

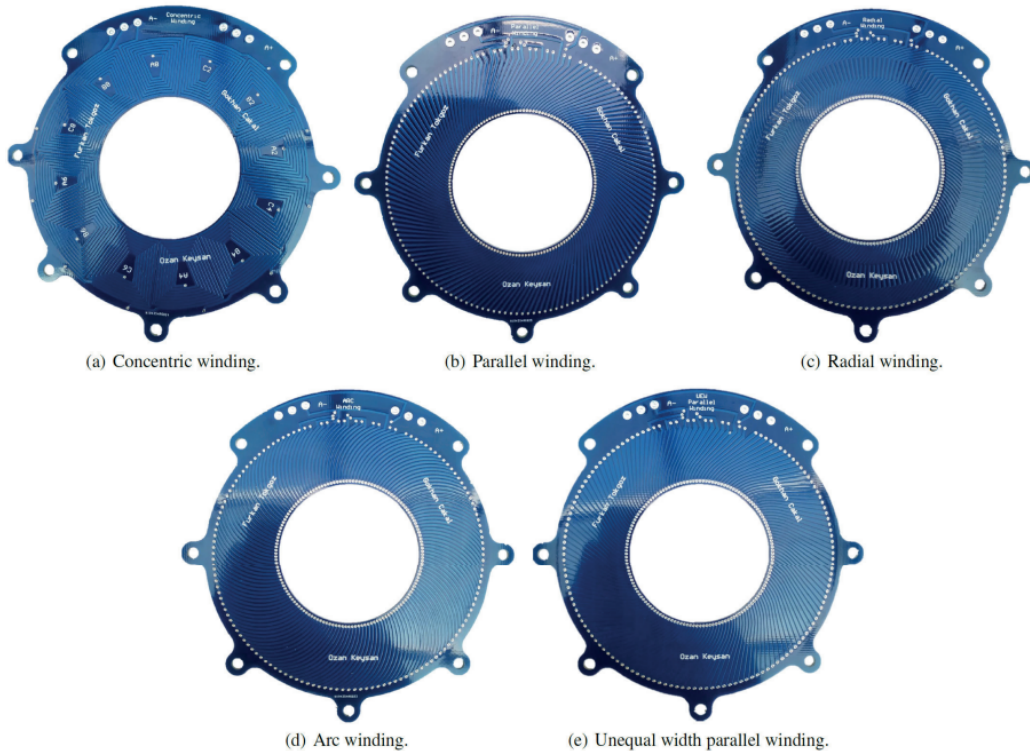


Figure 3.3: Types of PCB[2]

Current literature on PCB AFPMSMs predominantly explores spiral and rhomboidal PCB windings. However, these topologies face limitations, including reduced active conductor length, higher Joule losses, and suboptimal

utilization of the PCB surface exposed to the magnetic field. This led to the introduction of wave-type PCB windings, offering better utilization of the PCB's active surface area while minimizing Joule losses, an high current density and they can eliminate the cogging torque effect, reducing torque ripple[13].

Considering the spectrum of all these possibilities, prioritizing the need to obtain the torque required by the Team, it has been chosen the *non-overlapping radial wave type*:

- It suffers less from eddy currents compared to other topologies studied so far (arc, parallel, concentric, etc.).
- It exhibits low capacitive coupling (parasitic capacitance).
- It is less prone to overheating (which affects PCBs) due to better distribution, as they are also non-overlapping.
- In [12], a comparative analysis of wave-type PCB winding topologies for axial flux permanent magnet (AFPM) motors is cited, focusing on their back electromotive force (EMF), inductances, and torque production capabilities. The authors concluded that the non-overlapping radial wave winding exhibits the highest fundamental component of both the back EMF and electromagnetic torque.

3.2.1 Sizing equation

From the paper by Tokgoz [11], it is observed that, assuming infinite magnetic permeability in the yoke and neglecting any magnetic force drops in the yoke, the balance of the magnetomotive force (MMF) equations is given by:

$$4 \cdot H_m \cdot l_m + 2 \cdot H_g \cdot l_g = 0 \quad (3.25)$$

where H_m and H_g represent the magnetic field intensity in the magnets and the air gap, respectively.

In the analysis, for simplicity, it is assumed that the system exhibits no leakage or fringing flux. The following figure illustrates the magnetic field in the air gap as expected:

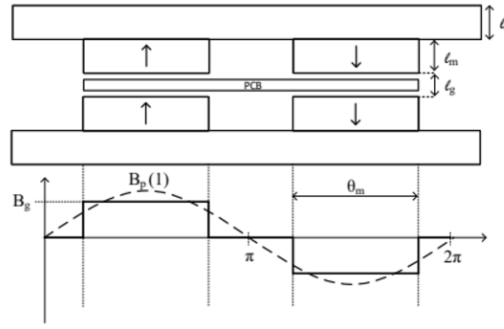


Figure 3.4: Magnetic field in the air gap

It is important to note that this assumption enhances the accuracy of the analysis when the magnetic air gap, l_g , is small. Consequently, the fluxes in the magnets and the air gap are considered equal, such that:

$$\phi_m = \phi_g, \quad (3.26)$$

where ϕ_m and ϕ_g denote the magnetic flux passing through the magnets and the air gap, respectively. Since leakage and fringing flux are neglected, the magnetic flux densities in the magnets, B_m , and the air gap, B_g , are also equal, yielding:

$$B_m = B_g. \quad (3.27)$$

The relationship between the magnetic flux density and the field intensity in the permanent magnets is expressed as:

$$B_m = \mu_0 \cdot \mu_r \cdot H_m + B_r, \quad (3.28)$$

where μ_0 is the air permeability, μ_r is the relative permeability of the permanent magnets, and B_r is the remanence flux density of the magnets.

By solving these equations collectively, the magnitude of the square-shaped flux density depicted in fig. 3.4 can be derived [11] and the magnetic flux density in the magnets and the air gap can be expressed as:

$$B_m = B_r \frac{2l_m}{2l_m + \mu_r \cdot l_g} \quad (3.29)$$

This result represents the fundamental component of the flux density in the air gap, which is subsequently used to derive the torque output.

The initial setup has been configured based on prior studies regarding the stator type. The main challenge lies in obtaining specific data necessary for determining the Lorentz force, torque, and ultimately, the output power. Calculating the Lorentz force and related parameters requires a value that can only be obtained through FEA analysis of the motor.

The equations identified for the design calculations, referenced from [13], are as follows:

$$A_m(r) = \frac{m_1 \cdot \sqrt{2} \cdot N_1 \cdot I_{ph}}{p \cdot \tau(r)}, \quad (3.30)$$

The current density (A_m) is computable once all parameters are determined from the matrix combinations in MATLAB. In order: m_1 is the number of phases, N_1 is the number of turns, I_{ph} is the phase current, p is the number of pole and $\tau(r)$ is the pole pitch that depends directly by the radius.

$$dF_x = A(r)(dS \times B_g), \quad (3.31)$$

leading to:

$$F_x = \alpha_i B_{mg} \int \frac{A_m(r)}{\sqrt{2}} 2\pi r dr, \quad (3.32)$$

where B_{mg} is independent of the stator radius, α_i is the ratio between the average to the peak value of the magnetic flux density. The integration is performed over the range r_{int} to r_{ext} and the current density formula is explicated.

$$F_x = \alpha_i B_{mg} \frac{2\pi}{\sqrt{2}} \int_{r_{int}}^{r_{ext}} \frac{m_1 \sqrt{2} N_1 I_{ph}}{p \tau(r)} dr, \quad (3.33)$$

which simplifies to:

$$F_x = \alpha_i B_{mg} m_1 N_1 I_{ph} \cdot [r_{ext} - r_{int}]. \quad (3.34)$$

Finally, once the Lorentz force is obtained, the electromagnetic torque generated by the winding in the PCB can be determined. The torque equation is given by:

$$dT = r \cdot dF_x \quad (3.35)$$

where r is the radial distance between the inner and outer radii of the stator.

$$dT = [k_{w1} \cdot A(r) \cdot B_{avg} \cdot dS] = 2\pi\alpha_i k_{w1} A(r) B_{mg} r^2 dr \quad (3.36)$$

where r is the radial distance, k_{w1} is the winding factor, $A(r)$ is the magnetic area, B_{avg} is the average magnetic flux density.

1 items

	Q	2p	kw	t	Ncpg	yq
1	480	20	0.955612	10	0.347826	24

Figure 3.5: Dolomites for PCB

To address this problem, a generator model was developed in MATLAB for FEA analysis using FEMM 4.2. Different MATLAB functions were implemented for the analysis automatization.

3.2.2 Parameters optimization

The sizing equation are reported at the end, due to the formulas consequences. Initially, a script was developed to identify the optimal solution for:

- the number of copper traces,
- the thickness of the copper traces,
- the spacing between the traces,
- the trace length.

The objective was to achieve a balance between Joule losses and a sufficiently high Lorentz force to obtain the torque requested of $12Nm$.

For the spacing between traces, several papers [13, 11, 14] suggest values in the range of 0.1 - 0.2 mm. Therefore, this range was adopted. Similarly, a range was selected for the trace thickness.

The number of traces is determined on the basis of the available space on the PCB, which is dependent on the parameters listed above. Finally, the trace length is approximated as a rectangle.

Parameters	Value	Unit
N° copper traces	$\approx 500 - 3500$	
Thickness copper traces	0.1-0.8	mm
Space between traces	0.1-0.2	mm
Trace length	65-80	mm
PCB thickness	2	mm
Airgap	2	mm

Table 3.1: Parameters

To explore all possible combinations of these parameters, MATLAB `ngrid` function was used to create a grid of variables (width, length, spacing, etc.). For each combination, the corresponding objective values (Joule losses and Lorentz force) were computed.

This solution was not successful, the losses were too high and the parameters were not optimized in the right way: clearly, the parameters set for optimization did not constrain Joule losses or the Lorentz force, resulting in parameters that lacked physical significance. An excessively high number of

tracks inevitably led to a track thickness and spacing that were not suitable for the problem.

3.2.3 Multi-Objective Optimization

The second chance shares the same characteristics as the previous one but aims to optimize inductance as well, through a multi-objective Pareto analysis.

In a multi-objective optimization problem, a candidate solution is Pareto optimal where no other feasible point exists that can improve one objective without worsening another. The analysis aims to find solutions where no further improvements can be made without creating trade-offs.

The Pareto solutions must not have any feasible descent directions that simultaneously improve all objective functions. There are two types of optimality: the Global Pareto optimality and Local Pareto optimality, which can become global under convex conditions.

Pareto optimality can be tested through mathematical optimization. Weakly Pareto optimal points exist when no other point has strictly lower values for all objectives simultaneously[15].

Also in this case, initially were trying to optimize the three parameters of track distance, trace width and trace length.

PCB	Parameters	Value
Number of Traces	500-3250	
Trace width	0.1 - 0.8	mm
Space between trace	0.1 - 0.2	mm
Trace length	65 - 80	mm
Airgap	2	mm
PCB thickness	2	mm

Table 3.2: First Range of parameters for PCB Design

First, a 2D analysis was conducted, so considering two parameters at a time, and subsequently a 3D analysis:

- Joule losses and Lorentz force
- Lorentz force and Inductance
- Inductance and Joule losses

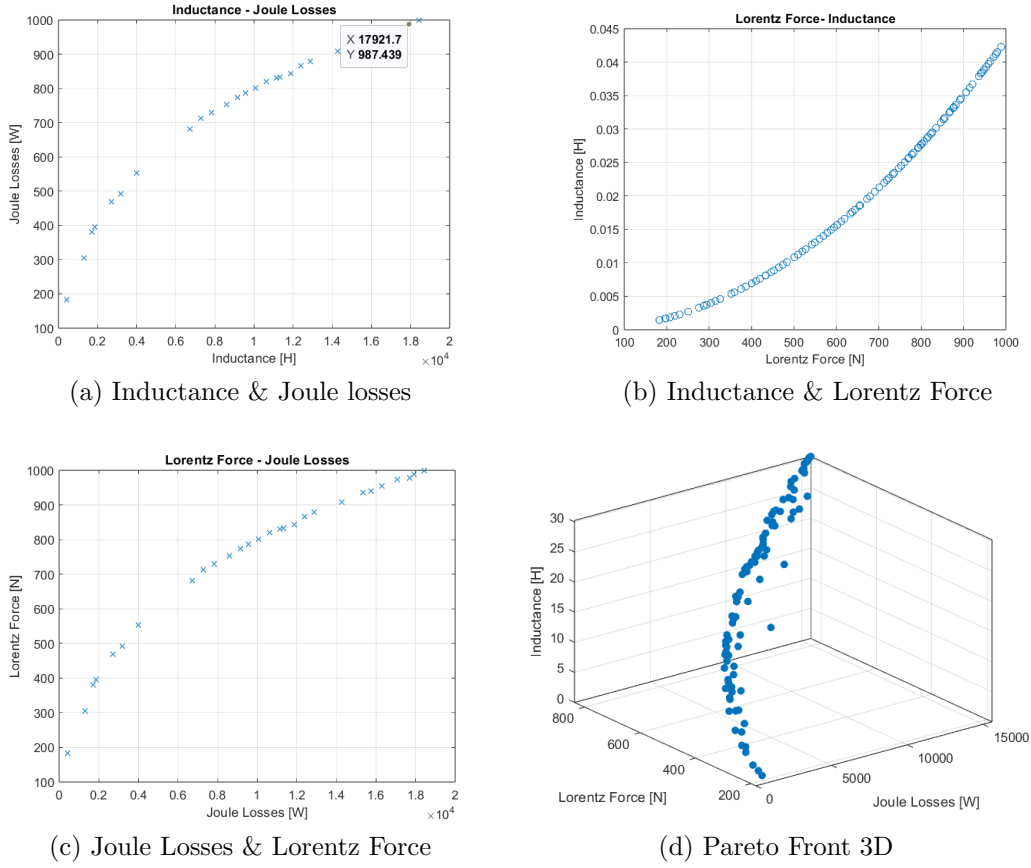


Figure 3.6: Pareto Front analysis

Also in this case, the results were not satisfying the target, the Joule losses and the inductance are too high to catch the desired solution. It was set as variables with a range for multi-objective analysis the distance between the traces, their thickness, and their length, and it was calculated the circumference to determine the PCB size. At this point, using the equation:

$$N_{turns} = \frac{circumference}{space + thickness} \quad (3.37)$$

there were obtained the number of turns available within the space defined by the circumference, for each configuration.

3.2.4 Final results

As mentioned before, the length and the copper width are the most important parameters. Finding the best solution, it was chosen another range of number

of traces, taken into account the multiplicity of the number of copper traces, because the simulation generates torque only when the number of stator windings per phase is a multiple of the number of pole and this implies that has to be a multiple of 60.

$$N_{traces} = pp \cdot m \cdot n \quad (3.38)$$

where pp is the number of poles, m the number of phases and n is the number of traces per pole per phases.

Since $n = 1, 2$ gives a very low value of Lorentz Force, it is not reported below, but the analysis is started from $n = 3$.

An approach that could significantly optimize the trace path could be finding a proper trade-off between trace length and the number of traces, in order to achieve sufficient Lorentz force and, consequently, a sufficiently high torque while maintaining a limited Joule losses.

Unlike the previous approach, the number of turns is no longer determined based on the available PCB space; instead, the trace thickness is designed according to the number of turns.

Parameters	Value	Unit
Number of Traces	180-480	
Trace width	0.1-0.8	mm
Space between trace	0.1-0.2	mm
Trace length	65-80	mm
Airgap	2	mm
PCB thickness	2	mm
Copper height	140	μm

Table 3.3: New Range of Parameters for PCB design

Based on this change, a graph was generated to illustrate how the parameters vary as a function of the number of turns, while consistently maintaining multi-objective optimization.

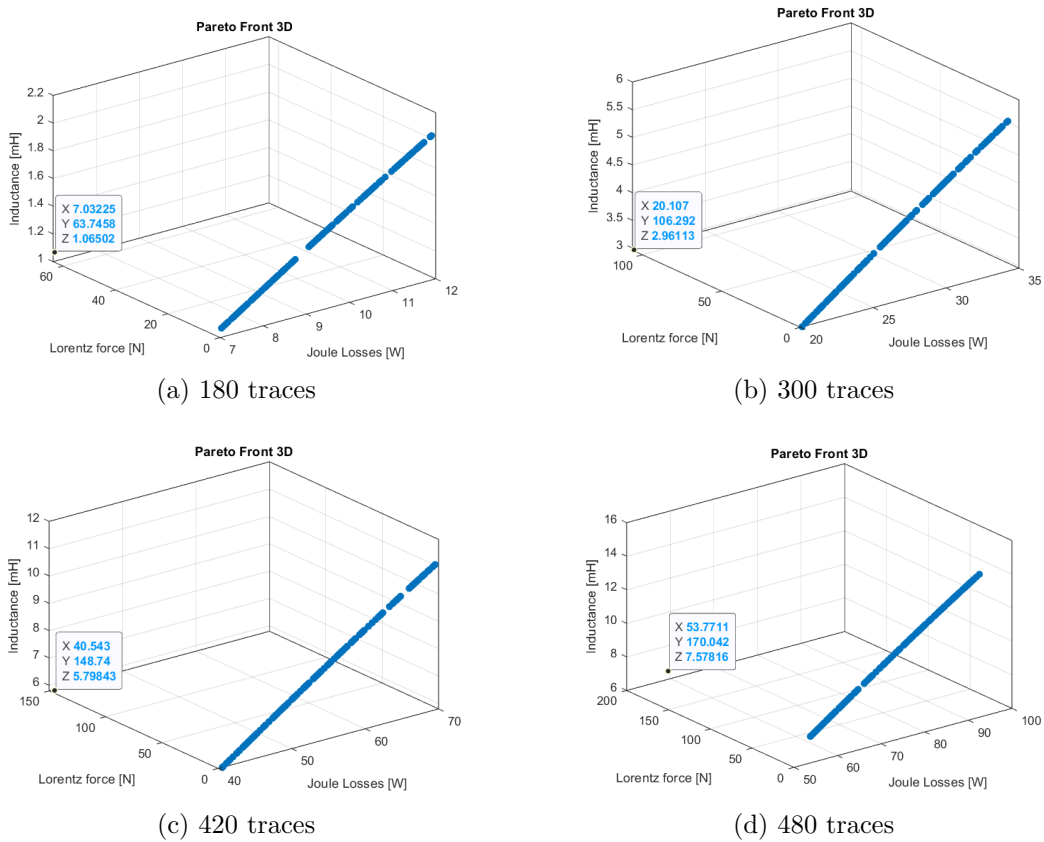


Figure 3.7: Number of traces for a single layer

The traces need to span a certain distance to reach the back side, which reduces the length along the radial direction. When fewer traces are used, they become wider and still need to cover the same distance to connect to the back. To properly make this connection, the traces would have to be significantly narrower. Excessive variations in width could lead to losses.[2]

These data belong to a single layer of PCB.

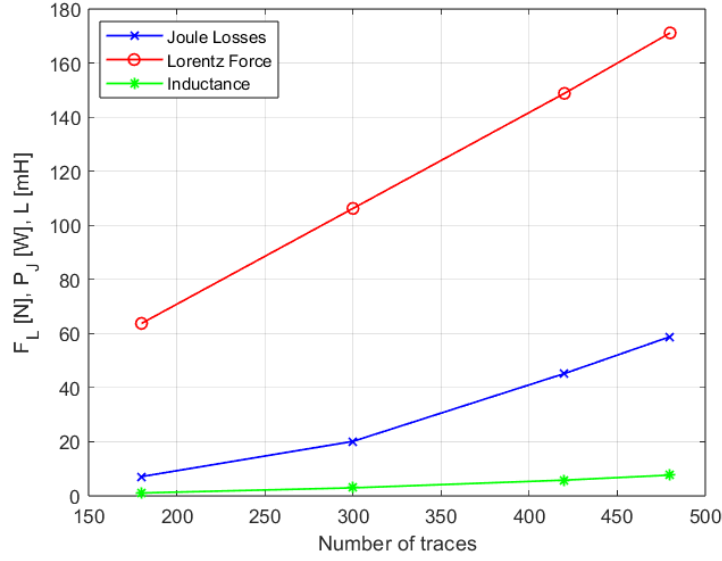


Figure 3.8: Trend with varying copper traces

The final proposed design involves a double-sided PCB and electrically connecting the layers in parallel. This ensures that the current is evenly distributed between the two layers. Additionally, if the two layers are made identical, the current will be divided uniformly. In this configuration, the total resistance of the path will be approximately half that of a single layer[12]:

$$R_{tot} = \frac{R_{single\ layer}}{2} \quad (3.39)$$

This approach may have thermal drawbacks: although the copper in both layers are identical, the heat generated by the top layer can affect the bottom layer, increasing local resistance, and vice-versa. Furthermore, due to differences in trace paths or via connections, the current may not be evenly distributed between the two layers, leading to local temperature increases and potential losses. The vias connecting the two layers must be sufficiently numerous and well-placed to avoid bottlenecks that limit the current flow between the layers.

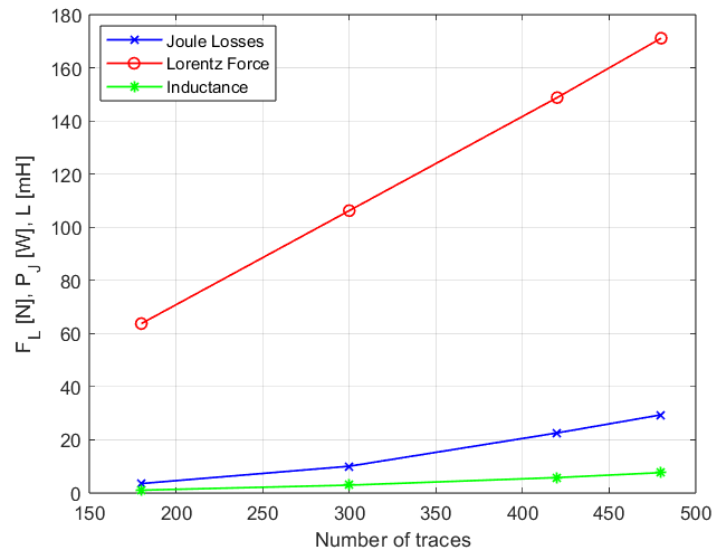


Figure 3.9: Trend with varying copper traces with double layer

To meet the specified requirements, it was decided to use 480 copper traces in order to achieve the desired torque, thereby generating the maximum Lorentz force.

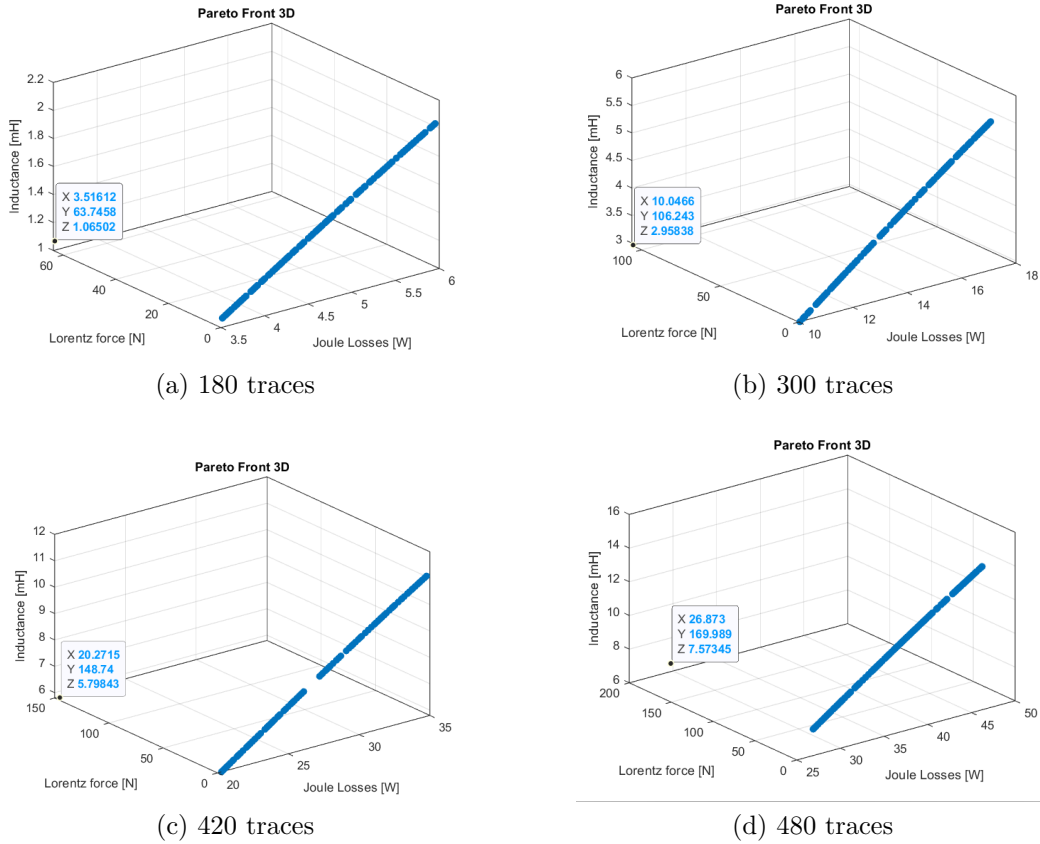


Figure 3.10: Number of traces for a double layer

At the end, the solution chosen does not depend anymore on the number of traces, but on the right compromise between the Joule losses and the Lorentz force balancing the length of the traces.

3.2.5 2D Analysis - FEA

Finite Element Analysis (FEA) is widely utilized in both industry and academia. Software implementing this method is often more intuitive than analytical modelling due to its graphical interface. FEA involves simulating a model using the finite element method, a mathematical approach applicable across various disciplines due to its robust computational capabilities.

The method works by dividing a structure into a finite number of elements, each assigned specific properties and interconnected via nodes, forming a computational grid. Depending on their dimensions, elements can be one-dimensional, 2D, or 3D, with unique parameters defined for each.

Today, numerous software tools implement this method. In this thesis, FEMM (Finite Element Method Magnetics) is implemented through MATLAB. FEMM offers the advantage of a highly graphical interface, making it easier to interpret and use[16].

Initially, the generator's geometry was designed with 10 pole pairs of N-S polarity and 480 PCB traces.

Within the simulation framework, when an external force rotates the rotor, it induces a varying magnetic flux through the stator windings. According to Faraday's law of electromagnetic induction, this varying flux generates a back electromotive force (EMF) in the windings. When the windings are connected to a load, the induced EMF drives a current through the stator.

In a 3D simulation model, the goal would be to represent a three-phase system where sinusoidal currents in the copper traces create a rotating magnetic field, synchronized with the permanent magnets positioned on the rotor. The current waveforms must exhibit sinusoidal profiles with precise phase shifts, and the magnet arrangement must produce a magnetic field aligned with these waveforms.

However, in this case, as the model is in 2D, the choice of performing a 2D simulation instead of a 3D one is primarily driven by computational efficiency and model simplicity. The 2D model allows for a faster simulation while maintaining reasonable accuracy.

Each magnet on the rotor has a specific polarity (North or South), which affects the magnetic field in proximity to the copper traces.

The entire generator structure was initially designed.

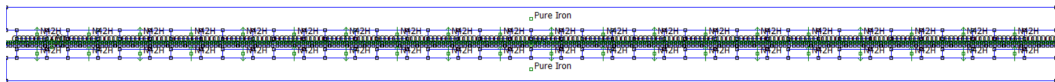


Figure 3.11: 2D model

Below a zoom on the central zone of the PCB, in order to see the traces, highlighting the double layer and the magnetization of the magnet.

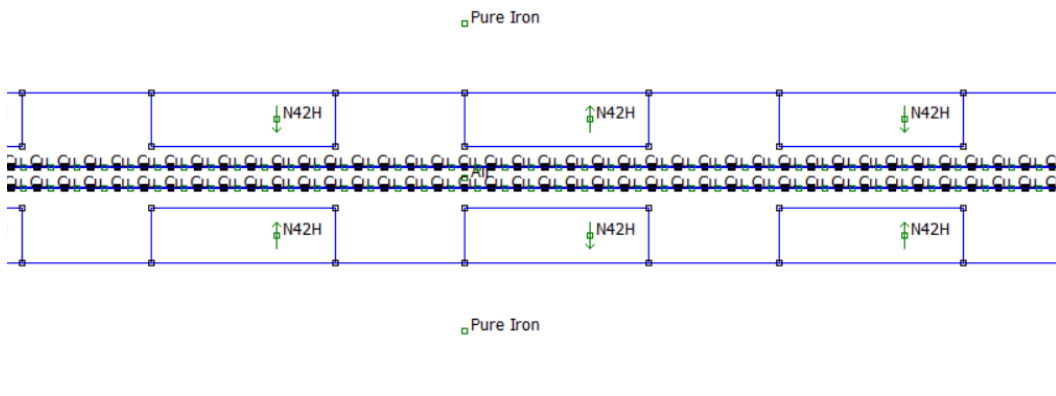


Figure 3.12: 2D details

The thesis [2] suggests, for simplicity, that to complete one electrical period, the rotor moves by two steps, allowing the windings to "see" both a north and a south pole. In fact, initially the simulation was conducted in this manner, but in order to show all the geometry, it has been chosen to show the complete design. The results are the same.

Boundary settings:

- Periodic boundary: the periodicity condition links the opposite edges of the domain. It is used to simulate that the left and right sides of the model are 'connected'. In FEMM, this type of condition is useful for models that repeat the same geometry periodically, such as in the case of a rotor or stator.
- Dirichlet boundary: The Dirichlet condition restricts the magnetic field output. It enforces that the magnetic flux does not exit the domain, making it useful for confining the field.

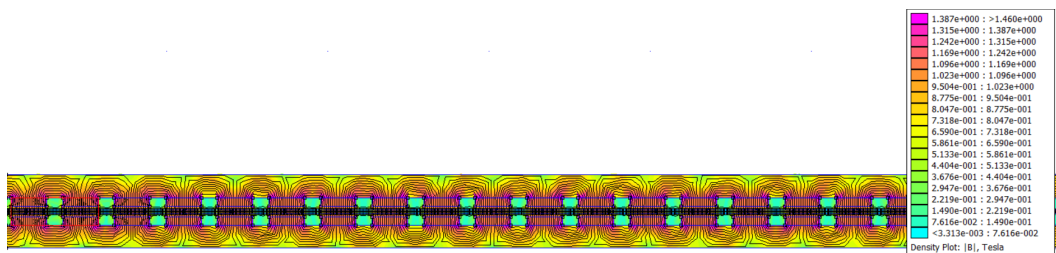


Figure 3.13: FEMM 2D

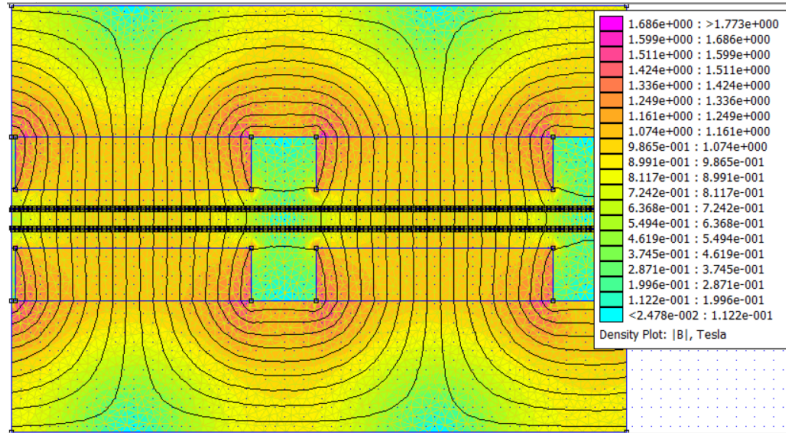


Figure 3.14: FEMM 2 poles

Thanks to this 2D model, it was possible to calculate the ratio between the peak induction and the average induction. By selecting 480 traces and a double-layer PCB, it follows that the torque will be

$$T \approx 12 \text{ Nm} \quad (3.40)$$

the power:

$$P_{elm} = \omega T = 433 \text{ W} \quad (3.41)$$

and the resistance:

$$R_f = 0.7335 \text{ } \Omega \quad (3.42)$$

Also in this case, it was calculated the magnetic flux:

$$\phi = 0.615 \text{ mVs} \quad (3.43)$$

and the linkage flux:

$$\lambda = N \cdot \phi = 0.0984 \text{ Vs} \quad (3.44)$$

With these results of the linkage flux and the magnetic flux (compared to 2.6), it is verified that the voltage limit is still respected at maximum speed.

During the optimization process to obtain the desired data, modifications were made to the code. For example, the thickness, which was initially a variable to be optimized in order to achieve a high value for the three unknowns (Lorentz Force, Joule losses, and inductance), became a fixed, chosen value. Ultimately, the optimization focused more specifically on the trace length to find a compromise between Joule losses and torque.

The main parameters used for sizing the stator are reported below:

Parameters	Value	Unit
Number of traces	480	
Trace width internal	0.3	<i>mm</i>
Trace width external	1.26	<i>mm</i>
Length	69	<i>mm</i>
Space between traces	0.1	<i>mm</i>
Resistance of a single trace	5.107	<i>mΩ</i>

Table 3.4: Final PCB design

To check the cost of the PCB and design the prototype, Altium was chosen. Altium is an advanced PCB design software widely used in the industry for its intuitive interface, powerful routing capabilities, and integration with simulation and manufacturing management tools. To route the tracks with the correct alternation, the schematic from Dolomites is used.

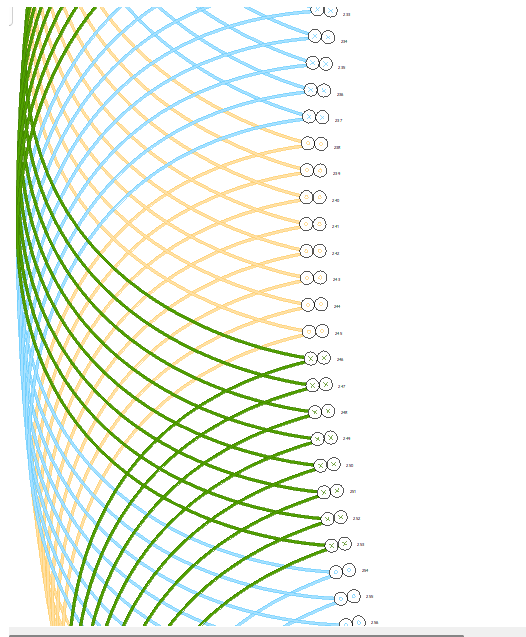


Figure 3.15: Windings PCB details with Dolomites

3.2.6 Design on Altium

Altium Designer is a leader PCB design software that integrates advanced routing technology, support for rigid-flex board design, and powerful data

management tools into a single, unified environment. This unified design environment streamlines the entire PCB design process, enhancing productivity and ensuring seamless transitions between design stages. With features like native 3D visualization, real-time cost estimation, and dynamic supply chain intelligence, Altium Designer empowers engineers to efficiently develop high-quality electronic products [17].

In order to adapt the configuration and to obtain a worthwhile values of torque and electric output power, according to the code, different thickness values have been adapted, varying as the circumference widens. All the traces are spaced as the code results, thick as calculated and the length is fixed as in tab. 3.4.

The traces were places through a code written in Pascal (annex in the Appendix 3.3), in order to have the traces perfectly assigned in the right space with the right distances.

In the figure below (see 3.16), it is possible to see, besides the traces, also the three current sensors, chosen from the website of Allegro Systems and the temperature sensor.

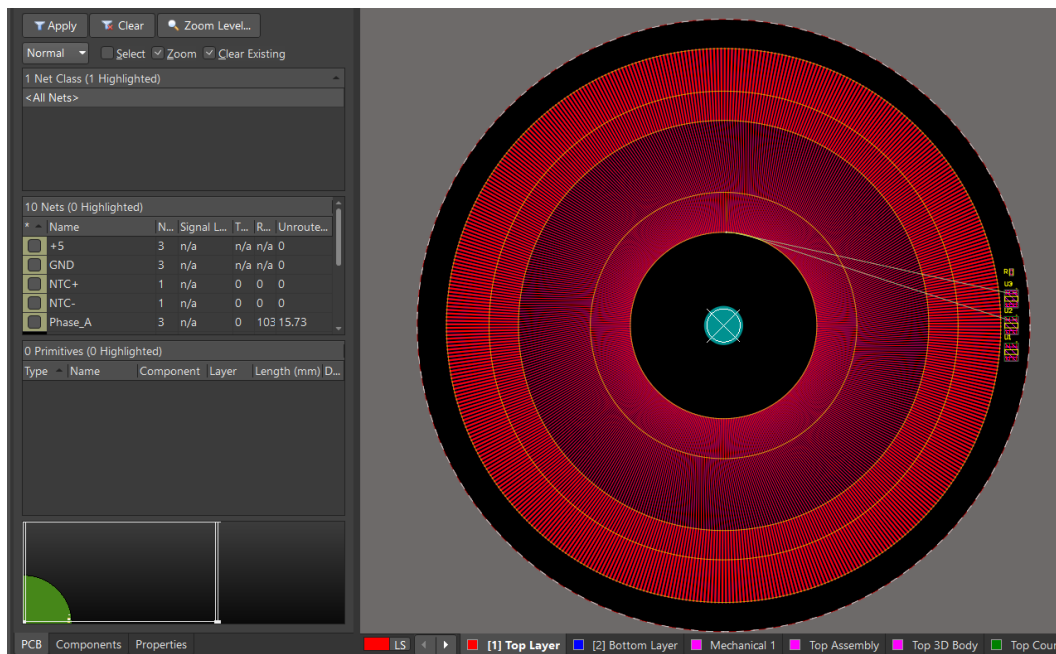


Figure 3.16: PCB with 480 traces on Altium

Actually, one of the advantages of the PCB stator is the easy implementation of the power electronics on the surface. For this reason, the hole is

maintained as the internal radius ($15mm$) of the previous stator, the dimension of the traces start from the external radius ($104mm$) and extend until the end of the length calculated. In the external ring, there is the space to place all the sensor desired and needed, see fig. 3.17.

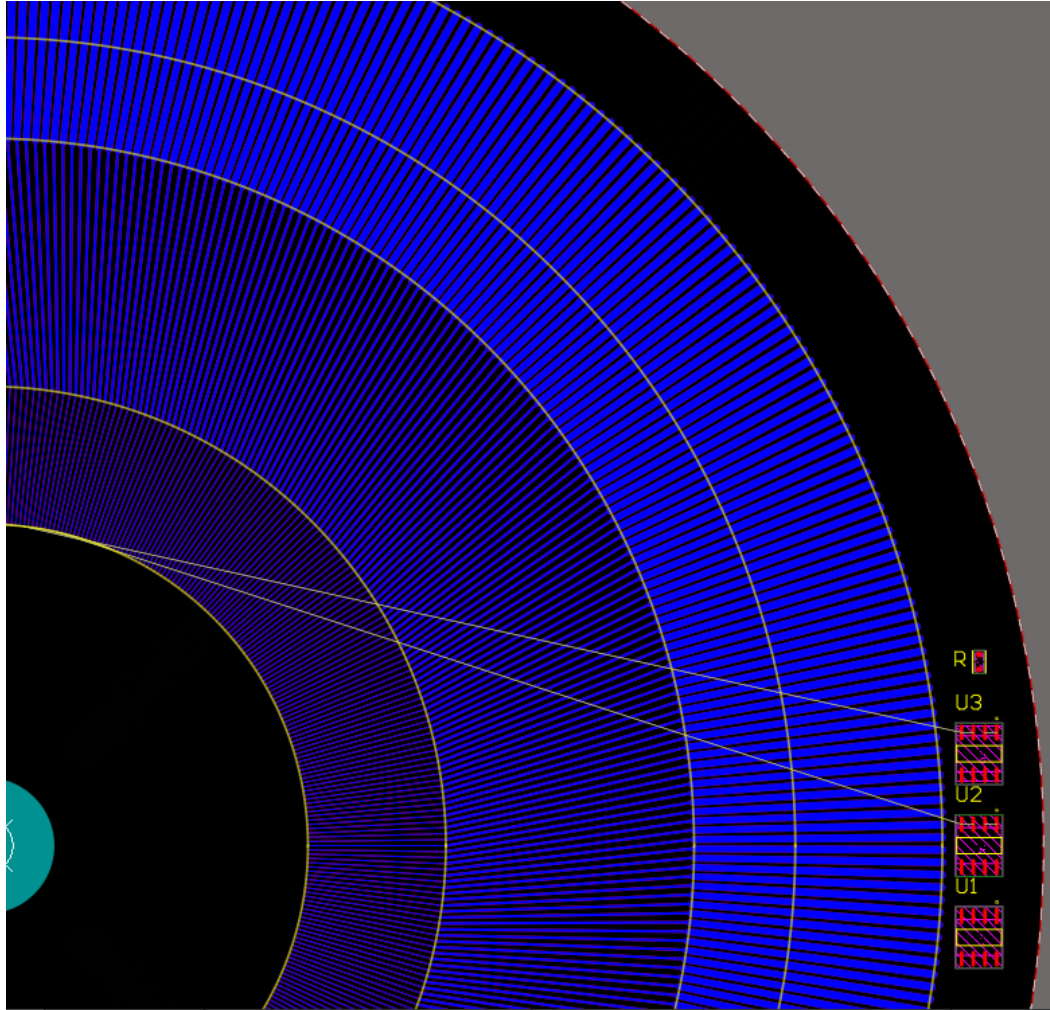


Figure 3.17: Detail of the sensors

Here reported the 3D view, in order to display the stator in a real view. The white circles are drawing used to design correctly all the traces.

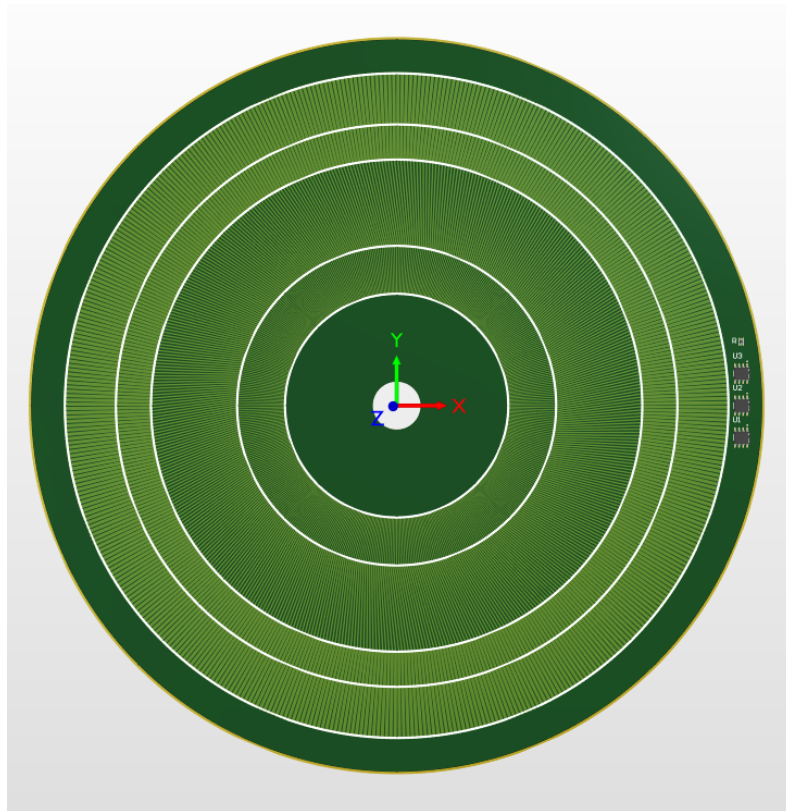


Figure 3.18: 3D view of Altium

Once the PCB stator was designed, it has been loaded on a web site to see the effective competitive price. Despite it is mandatory to order at least five pieces, it is possible to remain under one hundred of euros. Undoubtedly, a lower price compared to the manufacture of a coreless stator.

3.3 Technologies Comparison and Selection

By studying the pre-existing coreless stator through the thermal camera, it is possible to see that the windings are positioned as concentric PCB windings (see 3.3). Therefore, by comparing it to a PCB winding, and considering what has been stated previously, this type suffers from high Joule losses, adding that with high probability, the material used to wind the stator is not copper.

Reasoning about the optimized coreless stator, it has a phase resistance of 0.2Ω , while the measured real one is 1.673Ω , meaning there is an eightfold increase in resistance.

All considerations regarding Joule losses are made with the same current as

the Team Eolito generator in order to ensure a fair comparison in terms of Joule losses.

At this point, there are three main possible explanations:

1. The winding material is not copper: if it was aluminum, its resistivity is approximately 1.7 times that of copper. However, to obtain an eightfold increase in resistance, the wire would also need to have a smaller cross-section or a greater length. Since the winding follows the same geometry (the most common one for this type of generator), the material would have to be even worse than aluminum (perhaps an alloy with even higher resistivity).
2. If a thinner wire than expected was used, the resistance increases proportionally to $\frac{1}{A}$ (where A is the cross-sectional area of the wire). A wire with a cross-section approximately 8 times smaller than expected could explain the difference. It is likely that thinner aluminum was used to save weight and costs.
3. If the wire path in the windings is longer than anticipated in the studied design (for example, due to denser windings or a greater number of turns), the resistance increases. However, to achieve an eightfold resistance increase, the wire would need to be 8 times longer with the same cross-section and material, which is unlikely if the design is similar. Moreover, an increase in length could explain a moderate resistance rise, but not such a drastic one.

The most probable hypothesis is that the windings are made of aluminum with a reduced cross-section.

For this reason, in the optimization of the coreless stator, copper was obviously assumed as the material, and the windings remain concentric but with a different number of turns. This results in a significant reduction in losses and, consequently, a substantial increase in efficiency.

It is evident that in the PCB stator, Joule losses are higher (as it can be seen comparing fig. 3.19 and fig. 3.20) and the result is obviously that the efficiency is lower. This is because the number of traces is significantly higher to achieve

a useful torque value (see equations 3.17 and 3.40 with the respective values of power 3.18 and 3.41).

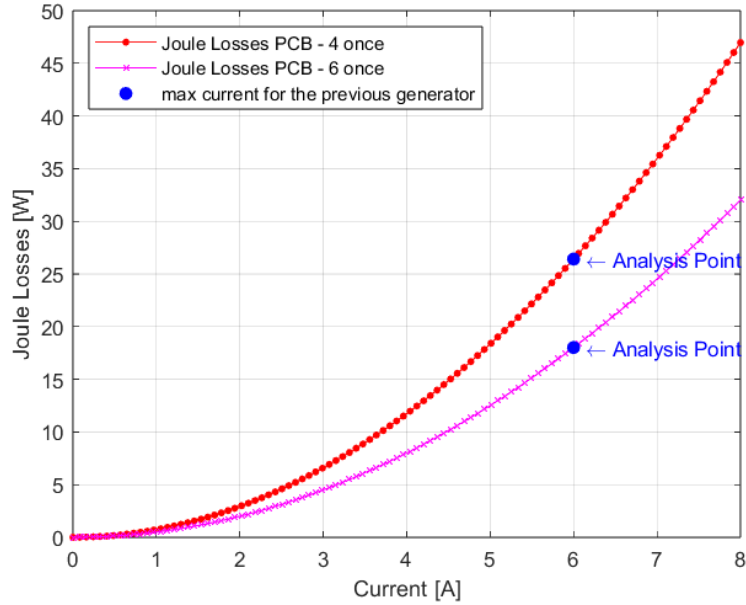


Figure 3.19: Joule Losses for PCB structure

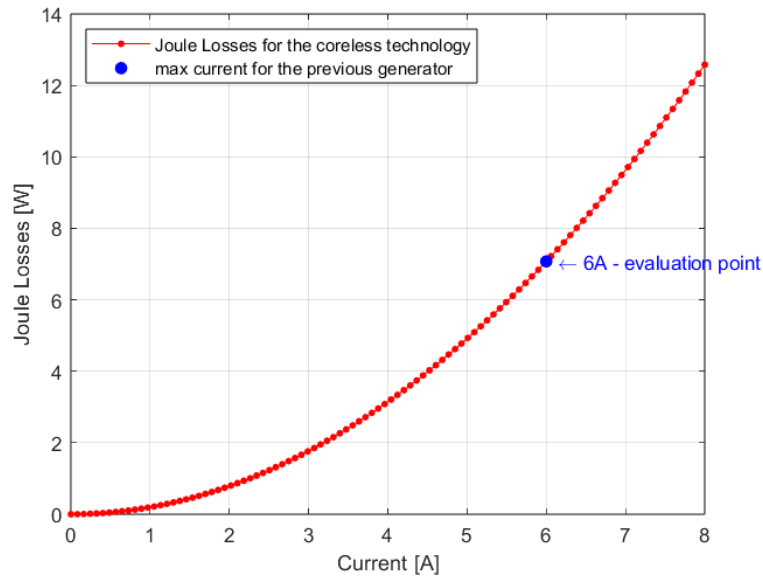


Figure 3.20: Joule Losses for coreless structure

It is evident (from figures 3.21a and 3.21b) that, in terms of both torque and power relative to speed, the coreless motor is more effective and has a

higher output. In terms of performance, it is clear that the comparison favors the choice of the coreless motor.

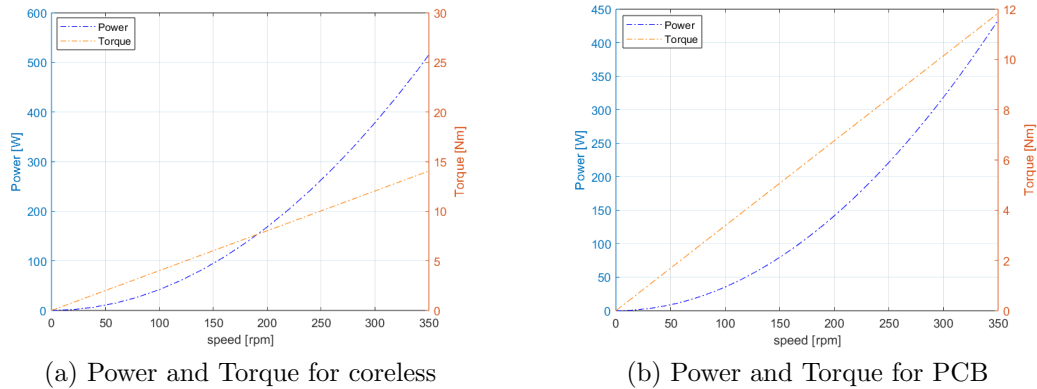
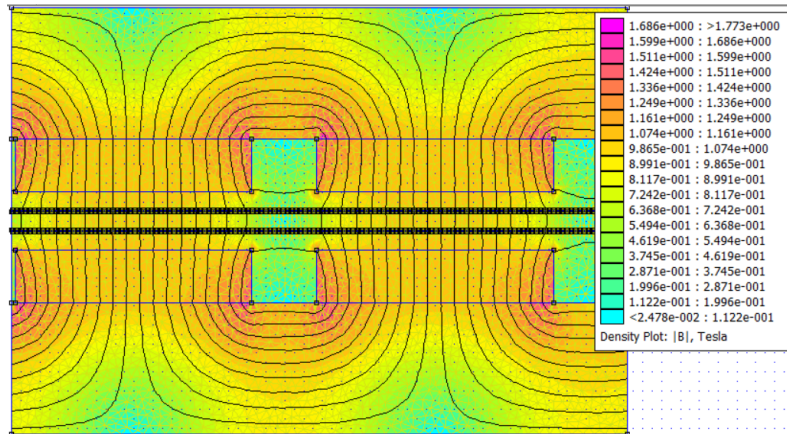


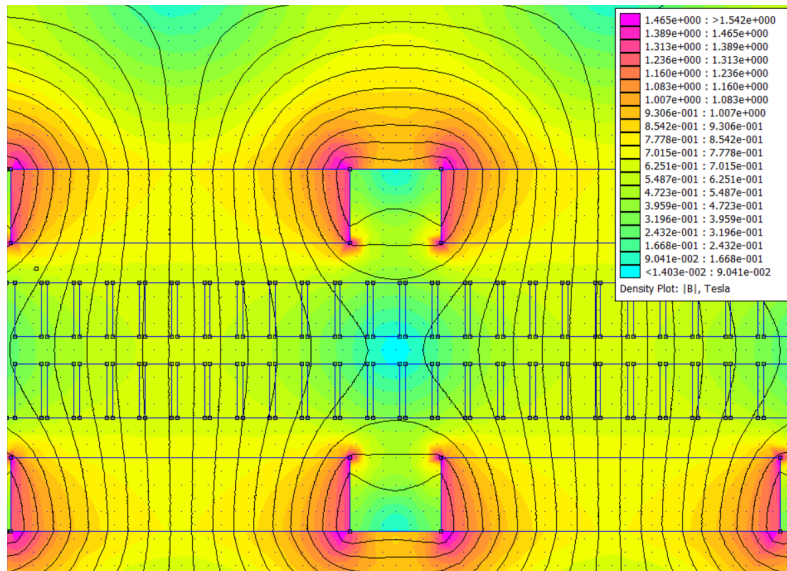
Figure 3.21: Comparison between the two technologies

Both undoubtedly suffer from negligible magnetic losses, thanks to the absence of a ferromagnetic core — eliminating both hysteresis and eddy current losses, provided that the spacing between traces is respected in the case of the PCB[18].

To obtain a clearer overall picture, the coreless generator was also modeled in FEMM to compare the two cases.



(a) Electromagnetic analysis for PCB



(b) Electromagnetic analysis for Coreless

Figure 3.22: Comparison between the two technologies for electromagnetic fields.

In both cases, the magnetic field is uniformly distributed, with slight saturation at the corners of the magnets. The magnetic field density is consistent with analytical calculations and the expected behavior of the generator.

Another advantage of the PCB is its lightweight nature, and it is even thinner than the coreless stator. In general, it can have multiple layers. In this specific case, among the unwritten requirements, a low budget had to be maintained. Naturally, the more layers there are, higher the cost and system complexity, also increasing the air gap.

In the coreless design, there is higher magnetic reluctance due to the absence of the core. A higher reluctance in a motor is generally negative, as it reduces the efficiency of magnetic flux transfer. Higher reluctance means that the magnetic circuit opposes the flow of magnetic flux, leading to weaker magnetic coupling between the rotor and stator. However, in reluctance motors (such as switched reluctance motors or synchronous reluctance motors), reluctance is intentionally exploited to produce torque. In these cases, reluctance variations are used to align the rotor with the lowest reluctance path, making it a useful property. For common motors like BLDC (Brushless Direct Current Motor), PMSM (Permanent Magnet Synchronous Motor), induction, lower reluctance is preferred to maximize performance and efficiency.

On the other hand, in the PCB, the estimated resistance is higher compared to traditional copper wire (due to the thinner copper traces). However, heat dissipation is more uniform thanks to the flat structure and the possibility of integration with heat sinks. Additionally, the low inductance reduces current ripple effects, which is useful for high-frequency applications, thus enabling higher speeds. Specifically, in this application, high speed values are not required. However, it is interesting to note that the speeds it can sustain are high, which is relevant for the future application of the generator. If, in the future, the rotor structure were to become more robust and capable of withstanding higher speeds, the PCB stator would be more adaptable to such changes without losing efficiency.

The coreless motor is lighter compared to a stator with a core but thicker than a PCB. It is more flexible in terms of design but requires a robust mechanical support to maintain structural integrity.

The PCB is much thinner and more compact, a huge advantage for applications in tight spaces: it reduces the overall weight of the machine. Another factor in which it is much more versatile than the coreless is that it is easier to integrate into advanced electronic systems. Still considering the versatility of the application, in addition to being more expensive due to the need for copper windings and epoxy resin, the coreless also has a more complex production process, as it requires specialized machinery and is more difficult to repair or modify. On the other hand, the PCB is more cost-effective in mass production due to standard PCB processes: high repeatability and precision in manufacturing.

The following table resumes a clearer comparison of the two more compact

stator topologies.

Feature	Coreless	PCB
Efficiency	Higher efficiency	Lower efficiency
Joule Losses	Lower due to larger wire cross-section	Higher due to smaller trace cross-section
Magnetic Losses	Negligible (absence of ferromagnetic core)	Negligible (absence of ferromagnetic core)
Weight	Lighter compared to stator with core	Lighter, thinner, and more compact, reducing overall weight
Thermal Dissipation	Less efficient, may trap heat without proper design	More uniform heat dissipation due to flat structure and easy integration of heat dissipation solution
Speed Capability	No high-speed requirement for this application	Can handle higher speeds, adaptable to rotor changes
Mechanical Support	Requires robust mechanical support for structural integrity	Thinner and more compact, less mechanical support required
Design Flexibility	Thicker than PCB and not flexible once designed	Easier to integrate into advanced electronic systems and more flexible for future improvement
Production Complexity	More complex (requires specialized machinery)	Easier to manufacture (standard PCB processes, high precision)
Cost	More expensive due to copper windings and epoxy resin	More cost-effective in mass production
Production in Tight Spaces	Thicker, less suitable for tight spaces	Ideal for applications in tight spaces due to compactness

Table 3.5: Comparison of Coreless and PCB Stators

Another aspect worth considering when testing various websites for ordering the PCB stator is that as the amount of copper increases, the price naturally rises as well — but not as much as one might expect.

In conclusion, it is important to study the adopted parameters:

Coreless	Parameters	Value
	Copper length	$42.78m$
	Section	$1.3mm^2$

PCB	Parameters	Value
	Copper length	$66.24m$
	Thickness	$140\mu m$ (4 ounces of copper)
	Maximum trace width (worst case)	$0.78mm$
	Section	$0.140mm \times 0.78mm = 0.1092mm^2$

Observation

The PCB requires a much longer conductor (PCB: $66.24m$ - coreless: $42.78m$), which increases the overall electrical resistance.

The coreless stator has a section about 12 times larger than the PCB trace (coreless: $1.3mm^2$ - PCB: $0.1092mm^2$).

This means that it is obvious that in the PCB the resistance will be much higher for the same material and temperature.

The PCB stator has about 4 times higher resistance compared to the coreless one. This results in higher Joule losses, which reduces efficiency.

In summary:

- Coreless: having a larger section, it dissipates less heat due to Joule effect. The resin insulation helps dissipation but could retain heat if not well-designed.
- PCB: the higher resistance means more thermal losses, which can cause heating. PCBs dissipate heat more uniformly over the entire surface, but the low copper section limits the ability to conduct high currents without heating.

A possible solution for PCB: increase the number of layers to reduce the resistance.

Optimize cooling with heat sinks or a sandwich design with thicker copper layers.

Increase copper thickness from 4 ounces to 6 ounces: the section becomes $0.210mm \times 0.69mm = 0.1449mm^2$. Joule losses go from $26W$ to $18W$, about a 30% decrease in losses. Additionally, using 6 ounces instead of 4 increases

safety for current flow since 6 ounces can handle 10–12A without overheating.

Apart from this adjustment, the idea of adding internal copper planes has been considered, as they are useful for:

- Better distributing the current, reducing localized heating in the thinner traces.
- Improving thermal dissipation, as the heat spreads over a larger area.
- Reducing overall electrical resistance, as current can flow through multiple parallel layers.

In this case, if the PCB carries about 8A, adding internal copper planes can help reduce the resistance of the main traces and improve thermal management.

After studying both the stators, it is evident that the coreless stator is more high-performance with respect to the PCB one.

Anyway, the choose be directed to the PCB stator:

- The losses are higher, but the system is absolutely at an high level of performance. The goal is reached: the output torque and the output power match with the requests of the team.
- The price is lower, that was a critical aspect of the demand, in order to avoid purchasing a new generator, thus maintaining a low budget.
- Lastly, considering that the Team is always changing the rotor structure, it is important to have a flexible generator, in order to follow the changes and the improvements.

For this reason, the PCB is the optimal choice: it could be improved with another layers if more torque or output power are necessary, but also it can handle higher speed, in case the rotor structure will be more endurance and so have to handle more wind speed.

Conclusions

This work focused on the design and optimization of an AFPMSG for a micro wind turbine, considering performance, cost, and manufacturability constraints. The benchmark study was necessary to confirm the assumption taken at the beginning: the existing generator did not reach the torque and efficiency requirements of the EoliTo team, particularly due to excessive Joule losses and consequently inadequate torque generation at low speeds.

Once established that the generator was not able to reach the value needed, it was clearly necessary to re-adapt the solution, but the challenge was above all to respect the low budget and at the same time improving the old generator with better performances.

To address these limitations, two stator configurations were analyzed: a coreless stator and a PCB stator. The coreless stator demonstrated higher performance in terms of torque and power, but was found to be less flexible for modifications and expensive to manufacture. The PCB stator, while slightly less efficient in absolute terms, provided significant advantages in terms of scalability, manufacturability, and cost reduction. Consequently, the final design choice was to implement the PCB stator, which was modeled in FEA with FEMM 4.2 and designed in Altium for rapid prototyping.

Despite the improvements achieved, the study highlighted some limitations. The PCB stator, while cost-effective, introduces higher electrical resistance due to the nature of PCB traces, which affect efficiency at higher power levels. Future work could focus on further optimizing trace layouts, exploring multi-layer PCB designs, or integrating cooling solutions to mitigate losses.

While the choice of a PCB stator was primarily driven by cost and ease of manufacturing, alternative approaches could be considered for future improvements. Optimizing the magnetic flux path, for example using Litz wire windings, or modifying the stator geometry could further enhance efficiency

and power output. However, these solutions would require a careful trade-off analysis to balance performance, manufacturability, and cost-effectiveness.

Overall, this research demonstrates that PCB-based AFPMSGs represent a feasible solution for cost-sensitive, low-speed (and not) wind power applications, balancing performance and affordability in a compact and efficient design.

Appendix

Here reported, in order, the datasheet of the magnets, the datasheet of the generator under study, the code in MATLAB for FEMM to draw the motor and the code to draw the windings on Altium with Delphi.

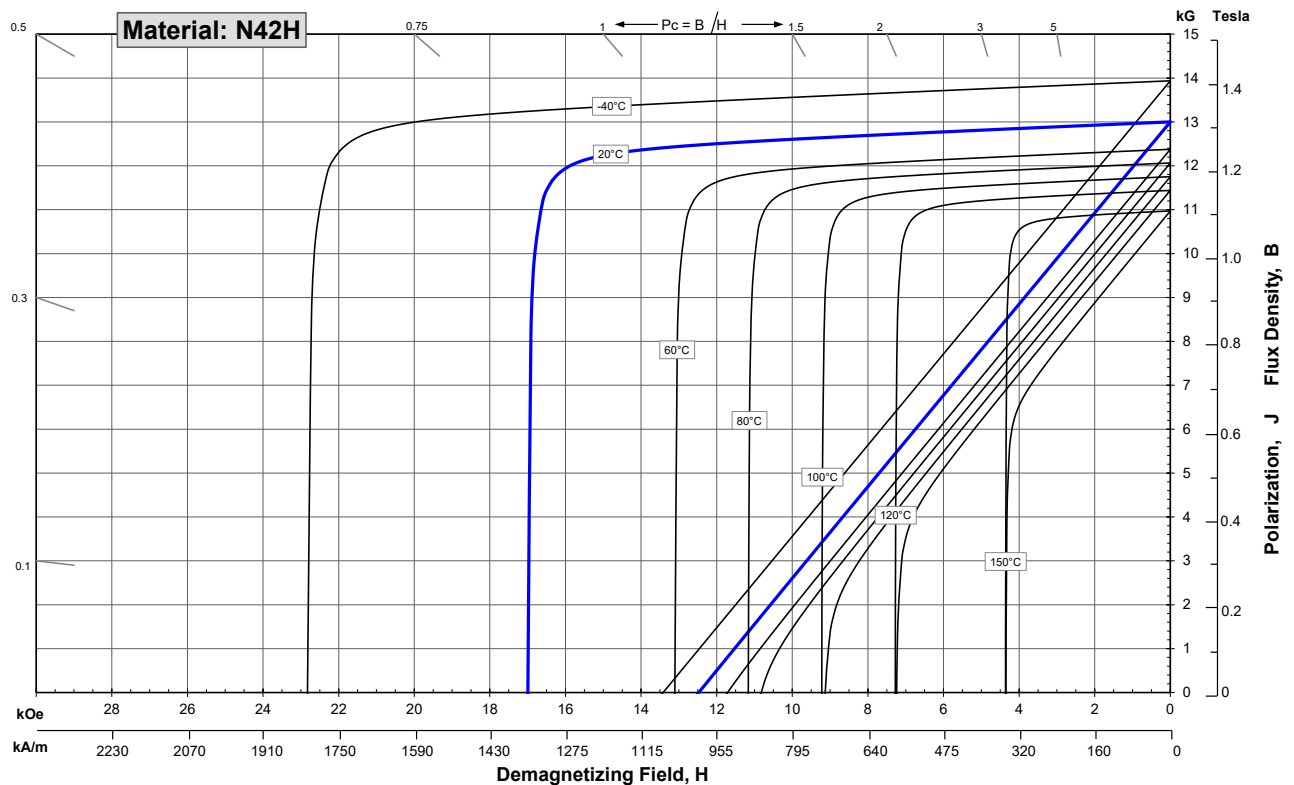
Sintered Neodymium-Iron-Boron Magnets

These are also referred to as "Neo" or NdFeB magnets. They offer a combination of high magnetic output at moderate cost. Please contact Arnold for additional grade information and recommendations for protective coating. Assemblies using these magnets can also be provided.

Characteristic	Units	Magnetic Properties		
		min.	nominal	max.
Br , Residual Induction	Gauss	12,800	13,000	13,200
	mT	1280	1300	1320
H_{cB} , Coercivity	Oersteds	12,000	12,300	12,600
	kA/m	955	979	1003
H_{cJ} , Intrinsic Coercivity	Oersteds	17,000		
	kA/m	1,353		
BH_{max} , Maximum Energy Product	MGOe	40	42	43
	kJ/m ³	318	330	342

Characteristic	Units	Thermal Properties	
		C //	C ⊥
Reversible Temperature Coefficients ⁽¹⁾	of Induction, α(Br)	%/°C	-0.12
	of Coercivity, α(H _{cj})	%/°C	-0.57
	Coefficient of Thermal Expansion ⁽²⁾	ΔL/L per °C×10 ⁻⁶	7
Thermal Conductivity	kcal/mh°C	5.3	5.8
Specific Heat ⁽³⁾	cal/g°C	0.11	
Curie Temperature, T _c	°C	310	
Other Properties	Flexural Strength	psi	41,300
		MPa	285
	Density	g/cm ³	7.6
	Hardness, Vickers	Hv	620
	Electrical Resistivity, ρ	μΩ • cm	150 // 130 ⊥

Notes: (1) Coefficients measured between 20 and 120 °C
 (2) Between 20 and 200 °C. Values are typical and can vary.
 (3) Between 20 and 140 °C



1 kA/m = 12.566 Oe 1 kOe = 79.577 kA/m

Notes The material data and demagnetization curves shown above represent typical properties that may vary due to product shape and size. **Demagnetization curves show nominal Br and minimum H_{cj}.** Magnets can be supplied thermally stabilized or magnetically calibrated to customer specifications. Additional grades are available. Please contact the factory for information.

TGET

—博冠·中国—

合肥博冠新能源技术有限公司
Hefei Top Grand Energy Technology Co., Ltd
www.china-topgrand.com Tel:86-551-65765201
E-mail: info@china-topgrand.com

1. MODEL: TGET260-I-0.25KW-200R

appearance is subject to change without notice



2. CHARACTER

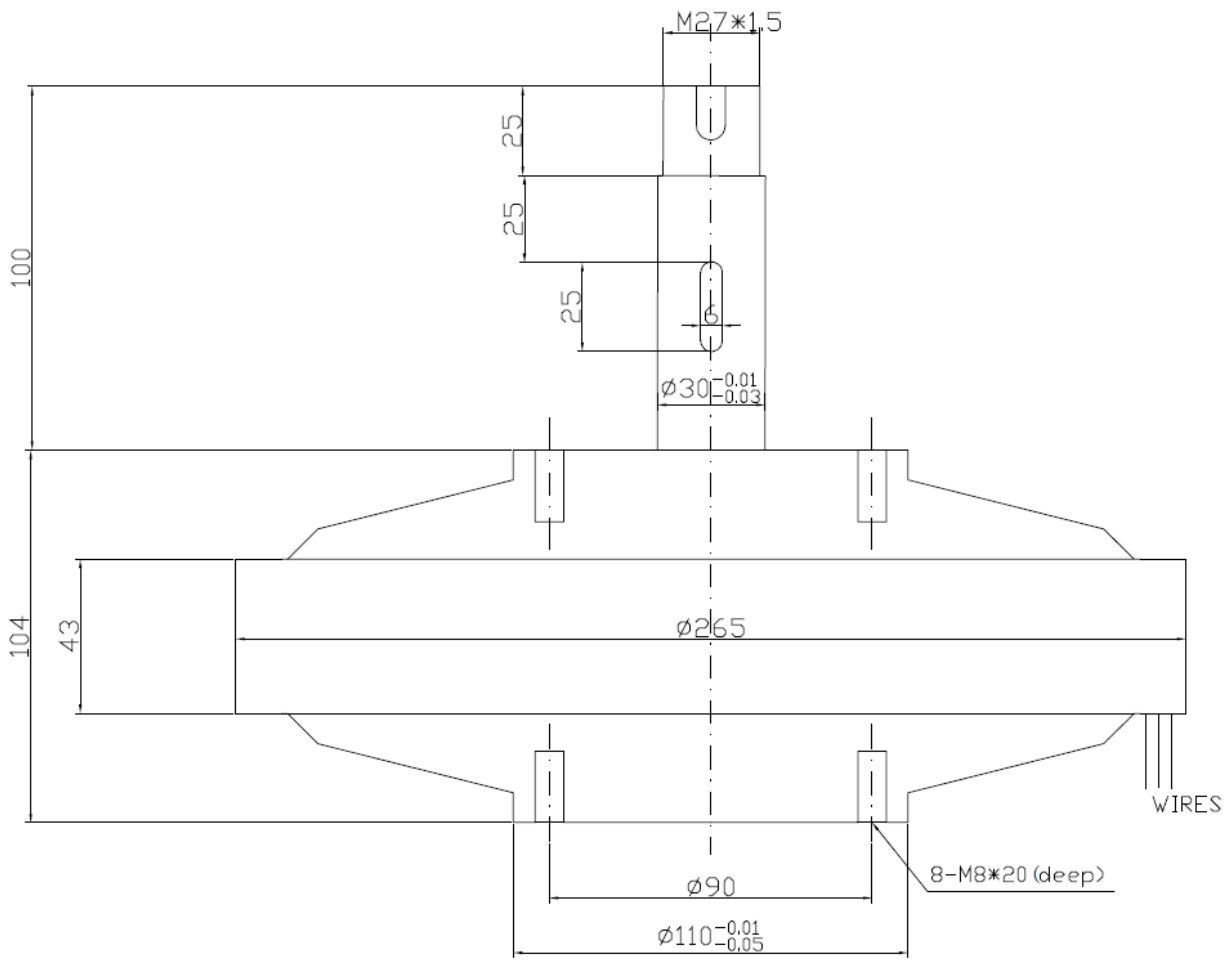
Our disc coreless PMG have advantage in low Rated speed, Low starting wind speed, Small volume, Energy Small, Light weight, Compact structure, High efficiency etc.

- 1) Coreless, anhysteresis, slotless, have low starting torque.
- 2) No iron loss, have high efficiency
- 3) Adopt unique coreless precision winding technology design precision coil
- 4) Adopt the rare earth permanent magnet, which is multipole, mean gap, high power density and high output power.
- 5) Low speed direct driving, no torque fluctuations
- 6) Compact structure, high ratio of power to volume
- 7) No iron loss, low calorific value, small temperature rise
- 8) Simple structure, easy to install
- 9) The brushless structure, free maintenance

3. RANGE OF APPLICATION

0.01-0.25kw vertical axis wind turbine; gasoline generators; hydroelectric generator

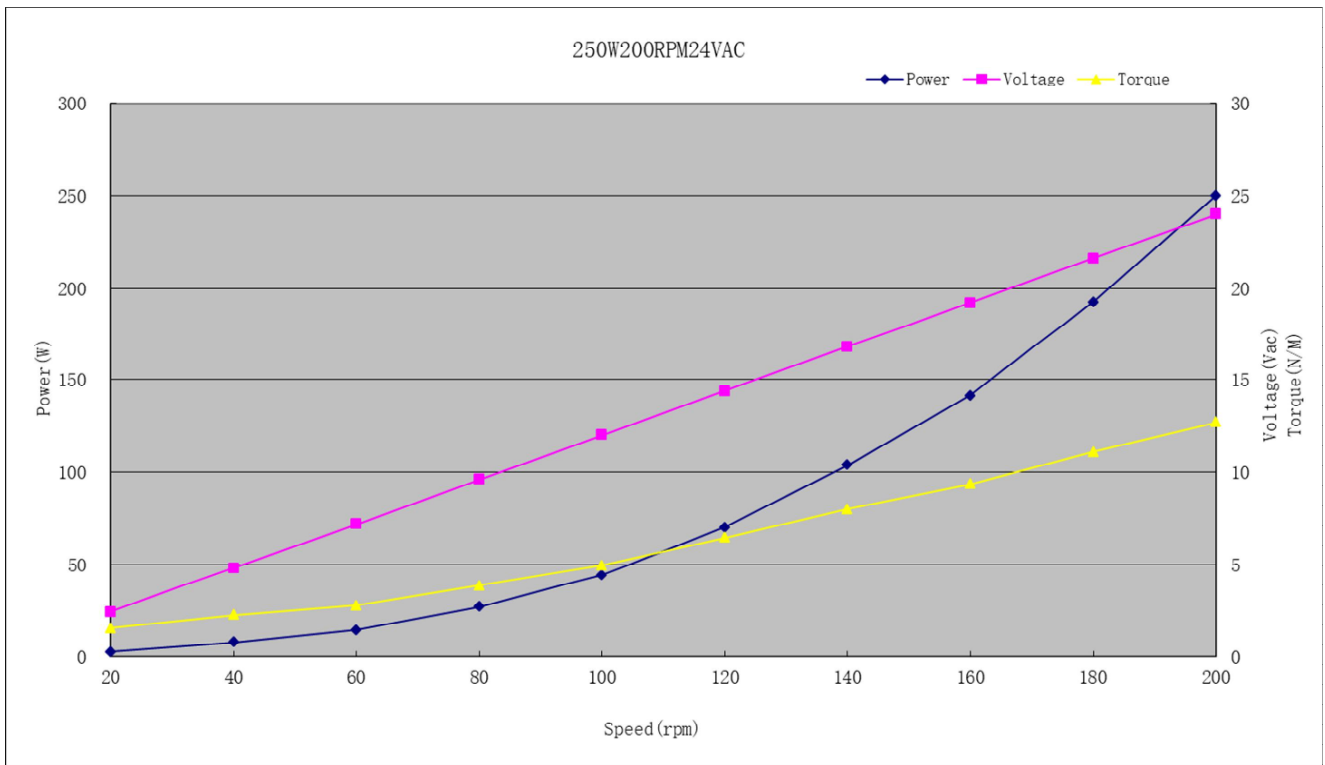
4. SHAPE DRAWING



5. PERFORMANCE PARAMETER

NO.	PARAMETER	UNITS	DATA
1	Rated power	KW	0.25
2	Rated speed	RPM	200
3	Rated voltage	V	24VAC
4	Rated Line Current		6.01A
5	Efficiency		>85%
6	Resistance (Line-Line)		-
7	Winding type		Y
8	Insulation Resistance		100Mohm Min(500V DC)
9	Leakage level		<5 ma
10	Start torque	N/M	<0.1
11	Phase		Three phase
12	Structure		Inner rotor
13	Stator		coreless
14	Rotor		Permanent magnet type (Inner rotor)
15	Housing Material		Aluminum (Alloy)
16	Shaft Material		Steel
17	Gen. Diameter	mm	265
18	Gen. Length	mm	104
19	Shaft. Diameter	mm	30
20	Net Weight	KG	13
20	Gross Weight	KG	16
Unit Price	USD430/PC FOB Shanghai (from 1PCS-10PCS)		
	USD415/PC FOB Shanghai (from 1PCS-10PCS)		

6. CURVE GRAPH



MATLAB code

```

1  %% Data: (all the measure are in millimeters)
f=58.33;           % frequency in [Hz]
In= 8.42;         % nominal current in [A]
Imax= 10;        % maximum current in [A]
h_mg= 5.5;       % height magnet in [mm]
6  dist_mg= 6.5;  % distance of two magnet in [mm]
h_airgap = 2;    % distance from the PCB stator to the
    magnet in [mm]
w_pcb= 2;        % standard thickness pcb in [mm]
r_pcb= 104*2*pi; % radius of pcb in [mm]
l_rotor= 104*2*pi; % radius of rotor in [mm]
11 h_rotor= 14;   % rotor height in [mm]
n_mg=20;        % number of magnet
d_mg = 25.5;    % magnet diameter
% Track:
n_traces=480;
16 l_cond= 0.3962; % axial lenght of a conductor in [mm]
h_cond=140e-3;   % height conductor in [mm]
dist_cond=0.0673; % distance from one conductor to another
    in [mm]
offset=(r_pcb-(n_traces-1)*(l_cond+dist_cond))/2;
offset_mg=(l_rotor-n_mg*(d_mg+dist_mg))/2;
21 %% Problem definition
openfemm;        % open FEMM
path='C:\choose_your_path';
newdocument(0)

26 name_fem = 'name_file_load';
mi_saveas([path,name_fem]);
mi_probdef(0,'millimeters','planar',1e-8,50,2); % Problem
    definition

%% INSERTION OF INSPECTION POINTS (2 rotors and 1 stator in
    PCB))
31 % pcb
mi_addnode(0,0);
mi_addnode(r_pcb,0);
mi_addnode(0,w_pcb);
mi_addnode(r_pcb,w_pcb);
36

```

```

%Insetion the copper conductors on the PCB above and below
k=1;
while k<n_traces
41 mi_addnode(offset/2+(k-1)*(l_cond+dist_cond),w_pcb);
mi_addnode(offset/2+(k-1)*(l_cond+dist_cond),0);

mi_addnode(offset/2+(k-1)*(l_cond+dist_cond),w_pcb+h_cond);
mi_addnode(offset/2+(k-1)*(l_cond+dist_cond),-h_cond);
46 mi_addnode(offset/2+k*1_cond+(k-1)*dist_cond,w_pcb);
mi_addnode(offset/2+k*1_cond+(k-1)*dist_cond,w_pcb+h_cond);
mi_addnode(offset/2+k*1_cond+(k-1)*dist_cond,0);
mi_addnode(offset/2+k*1_cond+(k-1)*dist_cond,-h_cond);
k=k+1;
51 end
%%
div=round(l_rotor/(d_mg+dist_mg));
"% This index is because you want there to be as many magnets
as could fit along the rotor""

56 k=1;
while k<div+1
% upper magnet
mi_addnode(offset_mg/2+(k-1)*(d_mg+dist_mg),w_pcb+h_cond+
h_airgap);
mi_addnode(k*d_mg+(k-1)*dist_mg,w_pcb+h_cond+h_airgap);
61 mi_addnode(offset_mg/2+(k-1)*(d_mg+dist_mg),w_pcb+h_cond+
h_airgap+h_mg);
mi_addnode(k*d_mg+(k-1)*dist_mg,w_pcb+h_cond+h_airgap+h_mg);
% lower magnet
mi_addnode(offset_mg/2+(k-1)*(d_mg+dist_mg),-(h_cond+h_airgap)
);
mi_addnode(k*d_mg+(k-1)*dist_mg,-(h_cond+h_airgap));
66 mi_addnode(offset_mg/2+(k-1)*(d_mg+dist_mg),-(h_cond+h_airgap+
h_mg));
mi_addnode(k*d_mg+(k-1)*dist_mg,-(h_cond+h_airgap+h_mg));
k=1+k;
end

71 % upper rotor
mi_addnode(0,w_pcb+h_cond+h_airgap+h_mg);
mi_addnode(0,w_pcb+h_cond+h_airgap+h_mg+h_rotor);
mi_addnode(l_rotor,w_pcb+h_cond+h_airgap+h_mg);

```

```

mi_addnode(l_rotor,w_pcb+h_cond+h_airgap+h_mg+h_rotor);
76 % lower rotor
mi_addnode(0,-(h_cond+h_airgap+h_mg));
mi_addnode(0,-(h_cond+h_airgap+h_mg+h_rotor));
mi_addnode(l_rotor,-(h_cond+h_airgap+h_mg));
mi_addnode(l_rotor,-(h_cond+h_airgap+h_mg+h_rotor));
81
%% Definition of the sides of the stator in PCB
mi_addsegment(r_pcb,0,r_pcb,w_pcb);
mi_addsegment(r_pcb,w_pcb,0,w_pcb);
mi_addsegment(0,w_pcb,0,0);
86 mi_addsegment(0,0,r_pcb,0);

%% Definition of the conductors in copper
k=1;
while k<n_traces
91 % upper conductors
mi_addsegment(offset/2+(k-1)*(l_cond+dist_cond),w_pcb,offset
/2+(k-1)*(l_cond+dist_cond),w_pcb+h_cond);
mi_addsegment(offset/2+(k-1)*(l_cond+dist_cond),w_pcb+h_cond,k
*l_cond+(k-1)*dist_cond,w_pcb+h_cond);
mi_addsegment(offset/2+k*l_cond+(k-1)*dist_cond,w_pcb+h_cond,k
*l_cond+(k-1)*dist_cond,w_pcb);
%mi_addsegment(k*l_cond+(k-1)*dist_cond,w_pcb,(k-1)*(l_cond+
dist_cond),w_pcb);
96 % lower conductors
mi_addsegment(offset/2+(k-1)*(l_cond+dist_cond),0,offset/2+(k
-1)*(l_cond+dist_cond),-h_cond);
mi_addsegment(offset/2+(k-1)*(l_cond+dist_cond),-h_cond,k*
l_cond+(k-1)*dist_cond,-h_cond);
mi_addsegment(offset/2+k*l_cond+(k-1)*dist_cond,-h_cond,k*
l_cond+(k-1)*dist_cond,0);
%mi_addsegment(k*l_cond+(k-1)*dist_cond,0,(k-1)*(l_cond+
dist_cond),0);
101 k=k+1;
end
%% Definition of lower conductors
k=1;
while k<div+1
106 mi_addsegment(offset_mg/2+(k-1)*(d_mg+dist_mg),-(h_airgap+
h_cond),offset_mg/2+(k-1)*(d_mg+dist_mg),-(h_airgap+h_mg+
h_cond));

```

```

mi_addsegment(offset_mg/2+(k-1)*(d_mg+dist_mg),-(h_airgap+
    h_cond),k*d_mg+(k-1)*dist_mg,-(h_airgap+h_cond));
mi_addsegment(k*d_mg+(k-1)*dist_mg,-(h_airgap+h_cond),k*d_mg+(
    k-1)*dist_mg,-(h_airgap+h_mg+h_cond));
% Definition upper magnets
mi_addsegment(offset_mg/2+(k-1)*(d_mg+dist_mg),w_pcb+h_airgap+
    h_cond,offset_mg/2+(k-1)*(d_mg+dist_mg),w_pcb+h_cond+
    h_airgap+h_mg);
111 mi_addsegment(offset_mg/2+(k-1)*(d_mg+dist_mg),w_pcb+h_airgap+
    h_cond,k*d_mg+(k-1)*dist_mg,w_pcb+h_cond+h_airgap);
mi_addsegment(k*d_mg+(k-1)*dist_mg,w_pcb+h_airgap+h_cond,k*
    d_mg+(k-1)*dist_mg,w_pcb+h_cond+h_airgap+h_mg);
k=1+k;
end

116 %% Definition of upper rotor
mi_addsegment(0,w_pcb+h_cond+h_airgap+h_mg,l_rotor,w_pcb+
    h_cond+h_airgap+h_mg);
mi_addsegment(0,w_pcb+h_cond+h_airgap+h_mg,0,w_pcb+h_cond+
    h_airgap+h_mg+h_rotor);
mi_addsegment(0,w_pcb+h_cond+h_airgap+h_mg+h_rotor,l_rotor,
    w_pcb+h_cond+h_airgap+h_mg+h_rotor);
mi_addsegment(l_rotor,w_pcb+h_cond+h_airgap+h_mg+h_rotor,
    l_rotor,w_pcb+h_cond+h_airgap+h_mg);
121 %% Definition lower rotor
mi_addsegment(0,-(h_airgap+h_cond+h_mg),l_rotor,-(h_airgap+
    h_cond+h_mg));
mi_addsegment(0,-(h_airgap+h_cond+h_mg),0,-(h_airgap+h_cond+
    h_mg+h_rotor));
mi_addsegment(0,-(h_airgap+h_cond+h_mg+h_rotor),l_rotor,-(
    h_airgap+h_cond+h_mg+h_rotor));
mi_addsegment(l_rotor,-(h_airgap+h_cond+h_mg+h_rotor),l_rotor
    ,-(h_airgap+h_cond+h_mg+h_airgap));
126 %% Definition of materials:
% PCB stator material dello statore and the airgap
mi_getmaterial('Air');
% Magnet material
mi_addmaterial('N42H', 1.05, 1.05, 1.353e6, 0, 0.0667, 0, 0,
    1, 0, 0);
131 % Copper conductors material
cond_Cu=58; %Copper conductivity
mi_addmaterial ('Cu',1,1,0,0,cond_Cu);
% Rotors material

```

```

mi_getmaterial('Pure Iron');
136 mi_getmaterial('1006 Steel');
    %% PCB material
mi_addblocklabel(r_pcb/2,w_pcb/2);
mi_selectlabel(r_pcb/2,w_pcb/2);
mi_setblockprop('Air',1,0,'',0,0,0);
141 mi_clearselected;
    %% Magnet material
k=1;
while k<div+1
    if mod(k, 2) == 0
146     %%upper
        mi_addblocklabel(d_mg/2+offset_mg/2+(k-1)*(d_mg+dist_mg),
            w_pcb+h_cond+h_airgap+h_mg/2);
        mi_selectlabel(d_mg/2+offset_mg/2+(k-1)*(d_mg+dist_mg),
            w_pcb+h_cond+h_airgap+h_mg/2);
        mi_setblockprop('N42H',1, 0, '',+90,0,0);
        mi_clearselected;
151     %%lower
        mi_clearselected;
        mi_addblocklabel(d_mg/2+offset_mg/2+(k-1)*(d_mg+dist_mg)
            ,-(h_airgap+h_cond+h_mg/2));
        mi_selectlabel(d_mg/2+offset_mg/2+(k-1)*(d_mg+dist_mg),-(
            h_airgap+h_cond+h_mg/2));
        mi_setblockprop('N42H', 1, 0, '', +90, 0, 0);
156     mi_clearselected;
    else
        %%upper
        mi_addblocklabel(d_mg/2+offset_mg/2+(k-1)*(d_mg+
            dist_mg),w_pcb+h_cond+h_airgap+h_mg/2);
        mi_selectlabel(d_mg/2+offset_mg/2+(k-1)*(d_mg+dist_mg)
            ,w_pcb+h_cond+h_airgap+h_mg/2);
161     mi_setblockprop('N42H',1, 0, '',-90,0,0);
        mi_clearselected;
        %%lower
        mi_addblocklabel(d_mg/2+offset_mg/2+(k-1)*(d_mg+
            dist_mg),-(h_airgap+h_cond+h_mg/2));
        mi_selectlabel(d_mg/2+offset_mg/2+(k-1)*(d_mg+dist_mg)
            ,-(h_airgap+h_cond+h_mg/2));
166     mi_setblockprop('N42H', 1, 0, '', -90, 0, 0);
        mi_clearselected;
    end
k=1+k;

```

```

end
171 %% Upper rotor material
mi_addblocklabel(l_rotor/2,w_pcb+h_cond+h_airgap+h_mg+h_rotor
/2);
mi_selectlabel(l_rotor/2,w_pcb+h_cond+h_airgap+h_mg+h_rotor/2)
;
mi_setblockprop('1006 Steel',1, 0, '', 0, 0, 0);
mi_clearselected;
176 %% lower rotor material
mi_addblocklabel(l_rotor/2,-(h_airgap+h_cond+h_mg+h_rotor/2));
mi_selectlabel(l_rotor/2,-(h_airgap+h_cond+h_mg+h_rotor/2));
mi_setblockprop('1006 Steel', 1, 0, '', 0, 0, 0);
mi_clearselected;

181 %% Airgap material
% upper
mi_addblocklabel(d_mg+dist_mg/2,w_pcb+h_cond+h_airgap/2);
mi_selectlabel(d_mg+dist_mg/2,w_pcb+h_cond+h_airgap/2);
186 mi_setblockprop('Air',1,0,'',0,0,0);
mi_clearselected;
% lower
mi_addblocklabel(d_mg+dist_mg/2,-(h_cond+h_airgap/2));
mi_selectlabel(d_mg+dist_mg/2,-(h_cond+h_airgap/2));
191 mi_setblockprop('Air',1,0,'',0,0,0);
mi_clearselected;

%% In this case not used, a three-phase system for the current
T = 1/f;
196 t = 0:40:2*T;
w = 2*pi*f;
ph_shift = 2*pi/3;

In = 0;
201 Ia = In * cos(w*t); % Fase A
Ib = In * cos(w*t - ph_shift); % Fase B
Ic = In * cos(w*t - ph_shift*2); % Fase C

% Definition of "positive and negative" sources
206 mi_addcircprop('A+', Ia, 1);
mi_addcircprop('B+', Ib, 1);
mi_addcircprop('C+', Ic, 1);
mi_addcircprop('A-', -Ia, 1);
mi_addcircprop('B-', -Ib, 1);

```

```

211 mi_addcircprop('C-', -Ic, 1);

% Definition of the current sequence in the easiest way
correnti = {'A+', 'A+', 'A+', 'A+', 'B-', 'B-', 'B-', 'B-', 'C
+', 'C+', 'C+', 'C+', ...
           'A-', 'A-', 'A-', 'A-', 'B+', 'B+', 'B+', 'B+', 'C
-', 'C-', 'C-', 'C-'};

216 % The traces
for k = 1:n_traces-1
    % Calculation of the trace position
    pos = l_cond/2 + offset/2 + (k-1)*(l_cond + dist_cond);

221 % Determine the current to assign to the current trace
    corrente = correnti{mod(k-1, 24)+1}; % Uso il modulo per
        ripetere ciclicamente la sequenza

% Add the corrispondent traces to each current
226 mi_addblocklabel(pos, w_pcb + h_cond/2);
    mi_selectlabel(pos, w_pcb + h_cond/2);
    mi_setblockprop('Cu', 1, 0, corrente, 0, 0, 0);
    mi_clearselected;

231 % Add the trace on the bottom side
    mi_addblocklabel(pos, -h_cond/2);
    mi_selectlabel(pos, -h_cond/2);
    mi_setblockprop('Cu', 1, 0, corrente, 0, 0, 0);
    mi_clearselected;

236 end
%% Boundary condition
mi_addboundprop('P_BCair_sopra', 0, 0, 0, 0, 0, 0, 0, 0, 4, 0
,0);
mi_addboundprop('P_BCair_sotto', 0, 0, 0, 0, 0, 0, 0, 0, 4, 0
,0);
mi_addboundprop('P_BCpcb', 0, 0, 0, 0, 0, 0, 0, 0, 4, 0 ,0);
241 mi_addboundprop('P_BCrotor_sopra', 0, 0, 0, 0, 0, 0, 0, 0, 4,
0 ,0);
mi_addboundprop('P_BCrotor_sotto', 0, 0, 0, 0, 0, 0, 0, 0, 4,
0 ,0);
% the right and left sides are connected through periodic
boundaries

% Add the region for the right segment

```

```

246 mi_addsegment(l_rotor, w_pcb+h_cond+h_airgap+h_mg, l_rotor,
      w_pcb); % definition of the airgap segment above
mi_addsegment(l_rotor, 0, l_rotor, -(h_cond+h_airgap+h_mg)); %
      definition of the airgap below
% Add the region for the left segment
mi_addsegment(0,w_pcb+h_cond+h_airgap+h_mg,0, w_pcb); % from
      the airgap to the upper magnet
mi_addsegment(0,-(h_cond+h_airgap+h_mg),0,0); % from the
      airgap to the lower magnet
251
% Definition of lateral right boundary

mi_selectsegment(l_rotor, w_pcb+(h_cond+h_airgap+h_mg)/2);
mi_setsegmentprop('P_BCair_sopra', 1, 0, 0, 0);
256 mi_clearselected;

mi_selectsegment(l_rotor, -(h_cond+h_airgap+h_mg)/2);
mi_setsegmentprop('P_BCair_sotto', 1, 0, 0, 0);
mi_clearselected;

261
mi_selectsegment(l_rotor, w_pcb/2);
mi_setsegmentprop('P_BCpcb', 1, 0, 0, 0);
mi_clearselected;

266
mi_selectsegment(l_rotor, -(h_cond + h_airgap + h_mg + h_rotor
      /2));
mi_setsegmentprop('P_BCrotor_sotto', 1, 0, 0, 0);
mi_clearselected;

mi_selectsegment(l_rotor, w_pcb+h_cond+h_airgap+h_mg+h_rotor
      /2);
271 mi_setsegmentprop('P_BCrotor_sopra', 1, 0, 0, 0);
mi_clearselected;

% definition of left boundary
276 mi_selectsegment(0, w_pcb+h_cond+h_airgap+h_mg+h_rotor/2);
mi_setsegmentprop('P_BCrotor_sopra', 1, 0, 0, 0);
mi_clearselected;

mi_selectsegment(0,w_pcb+h_cond+h_airgap/2);
281 mi_setsegmentprop('P_BCair_sopra', 1, 0, 0, 0);
mi_clearselected;

```

```

mi_selectsegment(0,w_pcb/2);
mi_setsegmentprop('P_BCpcb', 1, 0, 0, 0);
286 mi_clearselected;

mi_selectsegment(0,-(h_cond+h_airgap/2));
mi_setsegmentprop('P_BCAir_sotto', 1, 0, 0, 0);
mi_clearselected;
291

mi_selectsegment(0,-(h_cond+h_airgap+h_mg+h_rotor/2));
mi_setsegmentprop('P_BCrotor_sotto', 1, 0, 0, 0);
mi_clearselected;

296 mi_addboundprop('DirichletBC', 0, 0, 0, 0, 0, 0, 0, 0, 0); %
    A = 0
    % Dirichlet used to define the region where I am studying my
    % magnetic field

    %% Definition of the region above and below
mi_selectsegment(l_rotor/2, w_pcb+h_cond+h_airgap+h_mg+h_rotor
    );
301 mi_setsegmentprop('DirichletBC', 0, 1, 0, 0);
mi_clearselected;

mi_selectsegment(l_rotor/2, -(h_cond + h_airgap + h_mg +
    h_rotor));
mi_setsegmentprop('DirichletBC', 0, 1, 0, 0);
306 mi_clearselected;

```

Listing 3.1: MATLAB code for FEMM 4.2

Code Delphi

The following is the Delphi code used to create the precise windings.

```

const
  TiltAngle = 20.0; // Inclination angle in degrees
3 var
  Board: IPCB_Board;
  Track: IPCB_Track;
  CenterX, CenterY, Radius: TCoord;
  AngleStep, Angle, RadAngle, TiltRadAngle: Double;
8  NumTracks, i: Integer;
  Length, Thickness: TCoord;
  X1, Y1, X2, Y2: TCoord;
begin
  Board := PCBServer.GetCurrentPCBBoard;
13  if Board = nil then Exit;

  NumTracks := 480; // Number of segments
  AngleStep := 360.0 / NumTracks;
  CenterX := MilsToCoord(0);
18  CenterY := MilsToCoord(0);
  Radius := MilsToCoord(3779.53);
  Length := MilsToCoord(629.921);
  Thickness := MilsToCoord(39.33858);

23  for i := 0 to NumTracks - 1 do
  begin
    Angle := i * AngleStep;
    RadAngle := Angle * Pi / 180.0;
    TiltRadAngle := (Angle + TiltAngle) * Pi / 180.0; // Add
      inclination

28    // Calculation of the initial position
    X1 := CenterX + Round(Cos(TiltRadAngle) * Radius - (Length
      / 2) * Cos(TiltRadAngle));
    Y1 := CenterY + Round(Sin(TiltRadAngle) * Radius - (Length
      / 2) * Sin(TiltRadAngle));
    X2 := X1 + Round(Length * Cos(TiltRadAngle));
33  Y2 := Y1 + Round(Length * Sin(TiltRadAngle));

    // creating the track WITHOUT casting
    Track := PCBServer.PCBObjectFactory(eTrackObject,

```

```
        eNoDimension, eCreate_Default);  
    if Track = nil then Continue;  
38  
    Track.X1 := X1;  
    Track.Y1 := Y1;  
    Track.X2 := X2;  
    Track.Y2 := Y2;  
43    Track.Width := Thickness;  
    Track.Layer := eTopLayer;  
  
    Board.AddPCBObject(Track);  
end;  
48  
PCBServer.PostProcess;  
Board.ViewManager_FullUpdate;  
end;
```

Listing 3.2: Generation of Tracks with Inclination

Acknowledgments

Inizio ringraziando, primi tra tutti, i miei genitori, per aver sopportato ogni momento di “rispostacce” senza mai farle pesare e, anzi, strappandomi sempre una risata. Siete il mio cardine. Mio fratello che ha vissuto i pianti e i momenti felici in tutti questi anni: sei più di un amico, più di un fratello. Il nonno, che ascolta sempre i miei sproloqui su ciò che studio, e discute sempre con me sullo stato dell’arte delle tecnologie e dei progetti per il futuro, manco dovessimo decidere noi il futuro dell’umanità.

La mia famiglia al completo, perché belle così ce ne sono poche; la mia seconda famiglia, con cui ho avuto la fortuna di crescere: quella di Ale, che insieme da 20 anni non potrei definirla altrimenti, la tua famiglia è la mia e viceversa. Una sorella, una parte della mia vita così grande che non ricordo com’era la vita prima di te, letteralmente.

Per i miei amici la lista è infinita, quindi divido in sottocategorie, perché in fondo sono un’ingegnera anche io.

Per prima la mia coinqui, senza la quale questa tesi non sarebbe stata scritta, perché non mi sarei mai svegliata e spesso nemmeno nutrita, grazie mamma/-moglie/coinqui/sis cami di prenderti quotidianamente cura di me.

La mia piccola tribù dell’aula studio, quella precedente e quella passata, dagli “storici” a quelli che ho conosciuto nell’ultimo periodo: con voi studiare è stato proprio divertente; in particolare ringrazio i miei compagni di corso: senza di voi avrei capito la metà, fatto la metà e riso la metà.

Le mie due prime amichette del Poli, mai divise da niente, neppure da chilometri di distanza, stati diversi, botte date e pizzicotti, discussioni sulle cene tristi o i luoghi tristi dove mangiare e il costringervi ad uscire.

I miei due bambini, i miei siciliani preferiti e bodyguard noiosissimi: direi che la parte più difficile è stata istruirvi alle sezioni di gossip, probabilmente tanto difficile quanto il bene che vi voglio.

Infine, ringrazio anche i ragazzi del team Eolito, che con pazienza e determinazione hanno lottato con me affinché questo progetto potesse essere realizzato, ci vorrebbero più persone al mondo così.

Concludo con la citazione di un personaggio che - secondo la simpatica opinione di mio fratello - mi assomiglia:

“Questo progetto mi ha completamente confiscato la vita, tesoro. Mi ha consumato come solo un lavoro da eroe riesce a fare.

È il mio capolavoro, lo ammetto: semplice, elegante eppure importante.”

Bibliography

- [1] Bhuvaneshwari V and Carunaiselvane C. Characteristic stability analysis of axial flux motors in comparison with radial flux motors subjected to ev application. In 2023 IEEE International Conference on Power Electronics, Smart Grid, and Renewable Energy (PESGRE), pages 1–6, 2023. doi: 10.1109/PESGRE58662.2023.10404745.
- [2] Vincent Van den Eede Stijn Orleans. Design and construction of an electric motor with pcb stator and 3d printed housing, 2021. URL https://libstore.ugent.be/fulltxt/RUG01/003/014/883/RUG01-003014883_2021_0001_AC.pdf.
- [3] Arnold Magnetic Technologies Corp. Sintered neodymium-iron-boron magnets: N42h, 2021. URL <https://www.arnoldmagnetics.com/wp-content/uploads/2017/11/N42H-151021.pdf>. Accessed from provided PDF document.
- [4] S. Allirani, D. Shivashankaran, A.Sharuk Ahamed, and Velrajah Subaneshe. Simulation and fabrication of an axial flux permanent magnet synchronous motor. In 2022 International Conference on Augmented Intelligence and Sustainable Systems (ICAISS), pages 1319–1324, 2022. doi: 10.1109/ICAISS55157.2022.10010993.
- [5] Consulenza Tecnica Ing. Paolo Sordi Idrostech. Macchina a flusso assiale – equazioni fondamentali. <https://www.idrostech.com/afpm-axial-flux-electrical-machine/>, 2019.
- [6] M. Bonnet, J. F. Llibre, D. Harribey, and Y. Lefèvre. Ironless axial flux wind turbine motor with two cylindrical magnet rings. In 2022 International Conference on Electrical Machines (ICEM), pages 1941–1947, 2022. doi: 10.1109/ICEM51905.2022.9910802.

- [7] Stephane Ciciola. Types, performances and design of axial flux electrical machines for wind energy generation. Tesi di laurea magistrale, Politecnico di Milano, Milano, Italia, 2021/2022.
- [8] Nava Francesca. Sizing, optimisation and thermal evaluation of an axial flux permanent magnet motor in comparison with a radial flux motor. Master thesis, Politecnico di Milano, Milano, 2022/2023. Settore Scientifico Disciplinare: ING-IND/32 CONVERTITORI, MACCHINE E AZIONAMENTI ELETTRICI.
- [9] Adrian Augustin Pop, Mircea M. Radulescu, Horia Balan, Mihai Chirca, and Valentin Zaharia. Electromagnetic design and finite-element analysis of an axial-flux permanent-magnet machine. In 2014 International Conference on Applied and Theoretical Electricity (ICATE), pages 1–4, 2014. doi: 10.1109/ICATE.2014.6972638.
- [10] Bianchi Nicola Fornasiero Emanuele, Alberti Luigi and Bolognani Silverio. Considerations on selecting fractional-slot nonoverlapped coil windings. IEEE Transactions on Industry Applications, 49(3):1316–1324, 2013. doi: 10.1109/TIA.2013.2251853.
- [11] Furkan Tokgöz, Gökhan Çakal, and Ozan Keysan. Design and implementation of an optimized printed circuit board axial-flux permanent magnet machine. In 2020 International Conference on Electrical Machines (ICEM), volume 1, pages 111–116, 2020. doi: 10.1109/ICEM49940.2020.9271058.
- [12] Neethu Salim, Saurabh Prakash Nikam, Saumitra Pal, Ashok Krishnrao Wankhede, and Baylon Godfrey Fernandes. Multiphysics analysis of printed circuit board winding for high-speed axial flux permanent magnet motor. IET Electric Power Applications, 13(6):805–811, 2019. doi: <https://doi.org/10.1049/iet-epa.2018.5752>. URL <https://ietresearch.onlinelibrary.wiley.com/doi/abs/10.1049/iet-epa.2018.5752>.
- [13] S. Paul, M. Farshadnia, A. Pouramin, J. Fletcher, and J. Chang. Printed circuit axial-flux permanent magnet machines: A comparative analysis of their pcb topologies and performance characteristics. In 2018 IEEE

Bibliography

- International Magnetism Conference (INTERMAG), pages 1–1, April 2018. doi: 10.1109/INTMAG.2018.8508182.
- [14] Shahin Asgari, Nejat Saed, and Annette Muetze. Low-cost axial flux pcb motor with ferrite core and ferrite magnet topology for fan applications. In 2023 IEEE International Electric Machines & Drives Conference (IEMDC), pages 1–5, 2023. doi: 10.1109/IEMDC55163.2023.10238891.
- [15] Marco Sciandrone. Dipartimento di ingegneria dell’informazione, università di firenze, 2019. URL <https://webgol.dinfo.unifi.it/wp-content/uploads/2020/03/Dispmultiobiiettivo19.pdf>. Slide di un corso universitario.
- [16] FEMM Developers. Femm documentation, 2024. URL <https://www.femm.info/wiki/Documentation/>.
- [17] Altium. Altium designer documentation, 2024. URL <https://www.altium.com/documentation/altium-designer>. Accessed: 2025-02-18.
- [18] Murat G. Kesgin, Peng Han, Narges Taran, Damien Lawhorn, Donovan Lewis, and Dan M. Ionel. Design optimization of coreless axial-flux pm machines with litz wire and pcb stator windings. In 2020 IEEE Energy Conversion Congress and Exposition (ECCE), pages 22–26, 2020. doi: 10.1109/ECCE44975.2020.9236194.